Journal of Electron Spectroscopy and Related Phenomena 200 (2015) 193–208

Contents lists available at ScienceDirect

Journal of Electron Spectroscopy and Related Phenomena

journal homepage: www.elsevier.com/locate/elspec

Simulation of angle-resolved photoemission spectra by approximating the final state by a plane wave: From graphene to polycyclic aromatic hydrocarbon molecules

Peter Puschnig*, Daniel Lüftner

Institute of Physics, NAWI Graz, Karl-Franzens-Universität Graz, Austria

ARTICLE INFO

Article history:
Available online 17 June 2015

Keywords:
Density functional theory
Angle-resolved photoemission spectroscopy
Organic molecule
Organic–metal interface

ABSTRACT

We present a computational study on the angular-resolved photoemission spectra (ARPES) from a number of polycyclic aromatic hydrocarbons and graphene. Our theoretical approach is based on ab-initio density functional theory and the one-step model where we greatly simplify the evaluation of the matrix element by assuming a plane wave for the final state. Before comparing our ARPES simulations with available experimental data, we discuss how typical approximations for the exchange-correlation energy affect orbital energies. In particular, we show that by employing a hybrid functional, considerable improvement can be obtained over semi-local functionals in terms of band widths and relative energies of π and σ states. Our ARPES simulations for graphene show that the plane wave final state approximation provides indeed an excellent description when compared to experimental band maps and constant binding energy maps. Furthermore, our ARPES simulations for a number of polycyclic aromatic molecules from the oligo-acene, oligo-phenylene, phen-anthrene families as well as for disc-shaped molecules nicely illustrate the evolution of the electronic structure from molecules with increasing size towards graphene.

1. Introduction

Driven by the fact that the angular dependence of the photoemission current from oriented molecular films can be well-understood by assuming a *plane wave* as the final state of the photoemission process [1], a renaissance of *angular-resolved* photoemission spectroscopy (ARPES) in the field of organic electronics could be witnessed [2–6]. Thereby a technique, called *orbital tomography* [5,7–9], emerged which enables one to deconvolute photoemission spectra into individual orbital contributions. It can provide an orbital-by-orbital characterization of large adsorbate systems allowing one to directly estimate the effects of bonding on individual orbitals and also yields most stringent tests for ab initio electronic structure theory [5,10–12]. The reciprocal relationship between the ARPES intensity and the spatial distribution of the initial orbital has also been utilized to study the hybridization of molecular states with the substrate [13,14], explore intermolecular band dispersions [15,16,12], shed light on the role of intermolecular versus molecule-substrate interactions [17–19], determine molecular orientations [20–23], reveal the nature of doping-induced states [24], or even enable the reconstruction of molecular orbitals from ARPES data [4,25,26]. To date, however, the technique has been only applied to *molecular* adsorbate systems and the theoretical description has been based on ab-initio calculations for *isolated* molecules. In this work, we extend the theoretical description of the photoemission process to two-dimensionally periodic systems. As a prototypical example, we choose graphene and are able to demonstrate a seamless description of the electronic structure as observed by angle-resolved photoemission starting from molecular systems, poly-cyclic hydrocarbons, up to two-dimensionally extended systems, i.e., graphene.

Since graphene's first experimental realization, graphene research has expanded quickly leading to numerous groundbreaking experiments regarding the two-dimensional character of graphene. In quite simple terms, its electronic structure and mechanical stability is due the sp^2-hybridized valence electrons leading to three σ-bonds and one π-bond. The p_z electron makes up the π-bond, and is the key to the half-filled band that permits free-moving electrons. On the other hand, graphene can also be regarded as an infinitely large aromatic molecule, the limiting case of the family of flat polycyclic aromatic hydrocarbons (PAHs) [27],

* Corresponding author. Tel.: +43 3163805230; fax: +43 3163809820.
E-mail address: peter.puschnig@uni-graz.at (P. Puschnig).
URL: http://physik.uni-graz.at/ pep (P. Puschnig).

http://dx.doi.org/10.1016/j.elspec.2015.06.003

that is, hydro-carbon molecules composed of multiple aromatic rings, where biphenyl (2P) and naphthalene (2A) would therefore be considered as simple examples (Fig. 1).

The approach of the electronic structure of PAHs with increasing size towards graphene, or conversely, confinement effects in nano-graphene, have been the subject of numerous investigations. Starting from Clar's empirical aromatic π-sextet rule, the electronic and structural properties of various PAHs and nano-graphene can be understood [28–32] and the energetic stability of graphene nanoflakes and nanocones has been investigated [33]. In particular, graphene based quantum dots [34] and quantum-confined electronic states in graphene nanostructures [35] have been investigated. The wave functions and image potential states of graphene quantum dots could be mapped [36,37], or the confinement of Dirac electrons in graphene quantum dots have been observed [38]. With recent advances in ab-initio electronic structure theory, the geometric and electronic structures in the gas-phase have been screened for a comprehensive set of PAHs [39], a recent review on acene based molecules and materials can be found in Ref. [40].

Angle-resolved photoemission spectroscopy (ARPES) presents a powerful experimental tool to investigate the valence electronic structure of molecules. In order to unravel the full angular dependence of the photo-current, highly oriented films of molecules are a pre-requisite. In the past ten years, the growth of such highly-ordered molecular films, either as mono- or multilayers, could be demonstrated for a variety of PAHs on various substrates (see Ref. [41] an references herein). Specifically, much effort has been put on understanding the electronic structure of pentacene (5A) monolayers [42,25,43–45,12] and multi-layers [46–48,4] or that of other rod-like PAHs such as para-sexi-phenyl (6P) [3,4,14,24] or picene (5PA) [49,11]. But also disc-shaped PAHs, such as coronene (2DG) or hexa-benzo-coronene (3DG) have been the subject of ARPES investigations [8]. On the theoretical side, much progress could be made, once it was realized that for these systems, *i.e.* large π-conjugated hydro-carbon molecules, the final state of the photoemitted electron can be well approximated by a simple plane wave [3,4]. This allowed, for instance to gain information on the spatial electron charge distribution within individual molecular orbitals in good agreement with ab-initio electronic structure calculations [4,25] and similar in shape to images obtained by scanning probe techniques [50–52].

The success of using a simple plane wave for the final state for the description of the photocurrent from PAHs has been tied to three conditions [4]. First, π-orbital emissions from large planar molecules, second, an experimental geometry in which the angle between the polarization vector **A** and the direction of the emitted electron **k** is small, and third, the presence of only light atoms (H, C, N, O) which are expected to lead to small scattering cross sections. It is interesting to investigate whether the plane wave final state description can also be successfully applied to graphene as the limiting case of large PAHs. Experimentally, ARPES of graphene has been discussed extensively in the literature [53–56] and final-state effects in photoemission experiments from graphene on Ni(111) have also been discussed [57]. Early theoretical work on ARPES on graphite [58] suggest that plane waves indeed serve as a good approximation for the final state. This would be interesting since it allows for a reconstruction of graphene wave functions from ARPES data in an analogous way to what could already be demonstrated for molecules [25]. More precisely, the coefficients of Wannier functions can be determined from ARPES leading to images of the electron density in graphene [59]. As a first step towards this direction, the current manuscript explores how the orbital tomography approach can be applied to a two-dimensionally extended and strongly dispersing system such as graphene.

The paper is organized as follows. In Section 2 we present the computational set up of our calculations and outline the theoretical description of the photoemission intensity based on the one-step model and a plane wave final state. In the results section 3, we first summarize our DFT results in terms of orbital energies and (projected) density of states contrasting findings from a semi-local functional with those from a hybrid functional (Section 3.1). The remaining subsections are devoted to ARPES simulations which represent the main focus of the paper. First ARPES band maps as well as constant binding energies maps of graphene are presented and compared to available experimental data from the literature (Section 3.2). Then corresponding simulation results for oligo-phenyls (3.3), oligo-acenes (3.4), phen-anthrenes (3.5), and disc-shaped nano graphene (3.6) are presented where similarities and differences between the parent compound graphene and the molecular systems are highlighted. Finally, we give a conclusion in Section 4.

2. Theory

2.1. Density functional calculations

All theoretical results presented here are obtained within the framework of density functional theory (DFT) using the VASP code [60,61]. The projector augmented wave (PAW) method [62] has been used to account for the treatment of core electrons. We use two types of exchange-correlation functionals, namely the generalized gradient approximation (GGA) [63] or the range-separated hybrid functional HSE [64]. Preceding the computation of the electronic structure with either functional, all structures have been geometry-optimized using the GGA. Note that the oligo-phenyls have been constrained to be *planar* in order to allow for a better comparison with the other PAHs and graphene. Effects of non-planarity, i.e., inter-ring torsion angle, on the electronic structure of para-sexiphenyl are discussed in a separate publication [65].

All calculations for the molecules have been performed using a supercell with a minimum of 15 Å vacuum between the molecules' periodic replica. The graphene computations are performed for a free-standing layer with 30 Å distance between periodic layer replica.

2.2. Simulation of ARPES maps

The Kohn–Sham energies $\varepsilon_{n\mathbf{q}}$ and orbitals $\psi_{n\mathbf{q}}$ of the relaxed structures serve as input for the subsequent simulation of ARPES intensity maps within the one-step model of photoemission [66]. Here, the angle-resolved photoemission intensity $I(\theta, \phi, E_{\mathrm{kin}}; \omega, \mathbf{A})$ is a function of the azimuthal and polar angles θ and ϕ, respectively, the kinetic energy of the emitted electron E_{kin}, and the energy ω and polarization **A** of the incoming photon:

$$I(\theta, \phi, E_{\mathrm{kin}}; \omega, \mathbf{A}) \approx \sum_{n}^{\mathrm{occ}} \sum_{\mathbf{q}}^{\mathrm{BZ}} \left| \langle \psi_f(\theta, \phi; E_{\mathrm{kin}}) | \mathbf{A} \cdot \mathbf{p} | \psi_{n\mathbf{q}} \rangle \right|^2 \times \delta(\varepsilon_{n\mathbf{q}} + \Phi + E_{\mathrm{kin}} - \omega), \quad (1)$$

This formula can be viewed as a Fermi's golden rule expression, in which the photocurrent I results from a summation over all occupied initial states $\psi_{n\mathbf{q}}$, characterized by the band index n and Bloch vector **q**, weighted by the transition probability between the initial state and a final state. For the transition operator $\mathbf{A} \cdot \mathbf{p}$, the dipole approximation is assumed, where **p** and **A** are the momentum operator and the vector potential connected to the incoming photon. The δ function ensures energy conservation where Φ denotes the work function.

In the following, we approximate the final state ψ_f by a plane wave [1]. As outlined in more detail in a previous paper [4], and also noted earlier [58,67], this approximation allows us to greatly simplify the evaluation of the matrix element appearing in Eq. (1).

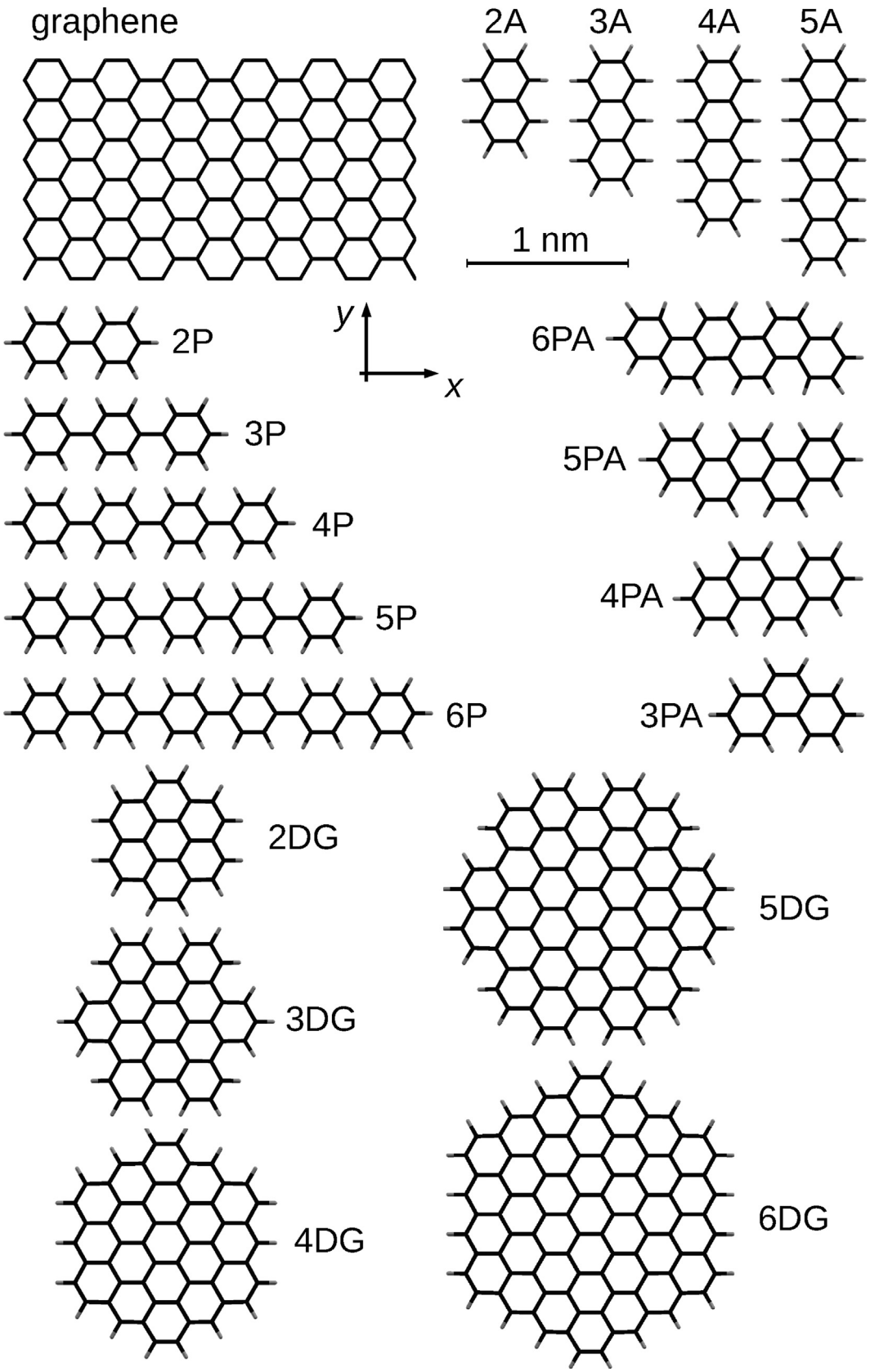

Fig. 1. Atomic structure of graphene and of the hydro-carbon molecules treated in this work: oligoacenes (*n*A), oligophenylenes (*n*P), phenanthrenes (*n*PA), and disc-shaped nano graphene (*n*DG). Note that all structures are to scale, and that the *x* and *y* axes have been chosen along the armchair and zig-zag directions of graphene, respectively.

If we denote the wave vector of the final, free-electron state by **k**, thus $E_{\mathrm{kin}} = (\hbar^2/(2m))k^2$, Eq. (1) simplifies to

$$I(k_x, k_y, E_{\mathrm{kin}}; \omega, \mathbf{A}) \approx \sum_{n}^{\mathrm{occ}} \sum_{\mathbf{q}}^{\mathrm{BZ}} \left|\mathbf{A}\cdot\mathbf{k}\right|^2 \left|\langle e^{i\mathbf{k}\mathbf{r}}|\psi_{n\mathbf{q}}\rangle\right|^2 \times \delta(\varepsilon_{n\mathbf{q}} + \Phi + E_{\mathrm{kin}} - \omega). \quad (2)$$

We obtain the simple result that the matrix element from a given initial state $n\mathbf{q}$ is proportional to the square modulus of the Fourier transform of the initial state wave function $\psi_{n\mathbf{q}}$ modulated by the weakly angle-dependent factor $|\mathbf{A}\cdot\mathbf{k}|^2$ which depends on the angle between the polarization vector **A** of the incoming photon and the direction **k** of the emitted electron.

We also see from Eq. (2) how the photon energy ω affects the photocurrent. When holding the initial state energy $\varepsilon_{n\mathbf{q}}$ constant, an increasing photon energy results in a larger final state energy E_{kin} and correspondingly final state wave number $|\mathbf{k}|$. Thus, the matrix element in Eq. (2) probes the Fourier transform of the initial state $\psi_{n\mathbf{q}}$ at a larger k-value as, for instance, illustrated by the Ewald-like sphere depicted in Ref. [4]. Due to the smooth and weakly varying k_z-dependence of σ and π orbitals of typical organic molecules, also the photon energy dependence of the simulated photocurrent is rather simple. Apart from the fact that with an increased photon energy a larger portion of the k space can be probed and that the overall intensity changes, the orbital-characteristic features in the $k_{\parallel}$ direction turn out to be quite insensitive to the choice of the photon energy in a range between 20 and 200 eV.

Note that Eq. (2) can be applied to single molecules as well as to extended systems such as organic layers adsorbed on metallic surfaces. In the former case the summation of the Brillouin zone (BZ) reduces to just one point, the Γ point, while for the latter situation, the possible dispersing bands are taken into account by the band structure $\varepsilon_{n\mathbf{q}}$ and Bloch states $\psi_{n\mathbf{q}}$ and an appropriate sampling of the Brillouin zone. For graphene, we used a lateral sampling 72×72 k-points which leads to a resolution of roughly $\Delta k = 0.035\,\text{Å}^{-1}$ in the ARPES spectra. Note that also for the ARPES simulations of the molecules, the Brillouin zones of the supercells have been sampled with typically $4 \times 4 \times 4$ k-points in order to achieve a comparable k-resolution in the ARPES simulations.

3. Results

3.1. Semi-local vs. hybrid functional

Before discussing the angle-resolved photo-emission cross sections of the systems depicted in Fig. 1, we study the role of the exchange-correlation functional on the electronic structure. In particular we compare the valence density of states (DOS) obtained within the generalized gradient approximation (GGA) [63] and the range-separated hybrid functional HSE [64] in Fig. 2. Panel (a) shows the DOS of graphene, while panels (b)–(e) depict the DOS of sexiphenyl (6P), pentacene (5A), picene (5PA), and of the disc-shaped nano graphene 5DG, respectively, *i.e.*, one representative of each class of molecules studied in this work.

Inspection of the graphene DOS reveals that the hybrid functional HSE leads to overall larger valence band widths compared to GGA, both for the π band (full, red line) as well as for the σ bands (dashed, blue lines). The GGA π band width is stretched from 7.7 eV to 9.0 eV when taking into account a fraction of exact exchange in the HSE functional. Similarly, the total σ band width is increased from 16.6 eV (GGA) to 18.3 eV (HSE). There is also a differential shift between π and σ states when comparing GGA and HSE, *i.e.*, σ states are pushed to larger binding energies compared to π states in the HSE. This trend, already well-known for several molecular systems, is due to the partial correction of self-interaction errors which are more pronounced in more localized σ states as compared to the more de-localized π states [68–70]. Regarding the position of the Fermi energy with respect to the vacuum energy, that is the work function, there is only little influence of the exchange-correlation functional, −4.28 eV (GGA) and −4.37 eV (HSE), a finding which is also to be expected.

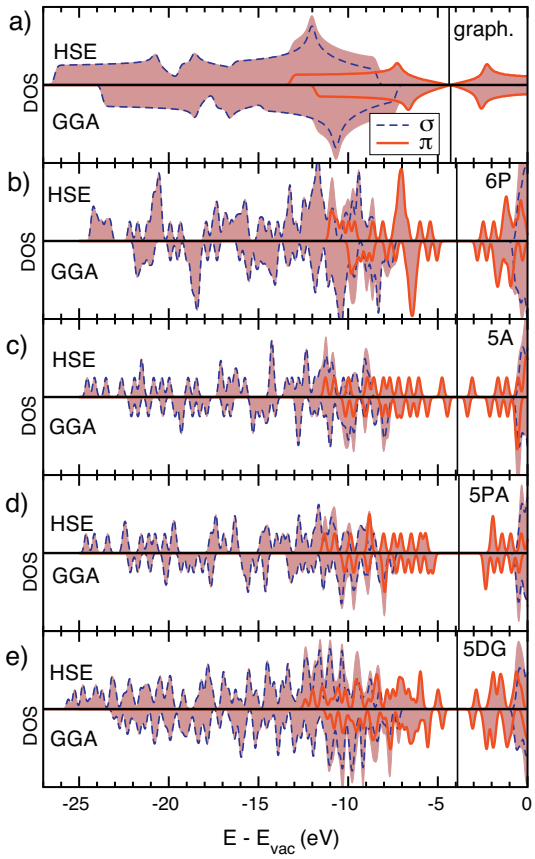

Fig. 2. (a) Comparison of the density of states for graphene calculated within HSE (top) and GGA (bottom), π and σ states are indicated by red solid and blue dashed lines, respectively. Energies are with respect to the vacuum level, the Fermi energy is indicated by the vertical line. Panels (b–e) show the corresponding data for 6P, 5A, 5PA, and 5DG. (For interpretation of the references to color in this figure legend, the reader is referred to the web version of the article.)

The DOS's of the molecular systems sexiphenyl (6P), pentacene (5A), picene (5PA), and 5DA are reminiscent of their parent compound graphene with similar binding energy ranges of the π and σ states. Also, the incorporation of a fraction of exact exchange in the HSE stretches the bands and pushes σ levels to larger binding energies compared to π states. Clearly, the overall band width of the valence π states is somewhat lower compared to graphene due to the finite size effects in the molecular systems. Here, 6P and 5PA have in fact similar HSE π band widths of 5.55 eV and 5.62 eV, respectively, while 5A has a considerably larger value of 6.55 eV. This can be rationalized by the fact that oligo-acenes can be viewed as a graphene snippet with zig-zag termination, that is along a direction which encompasses the Dirac point along the $\Gamma - K$ direction, while 6P and 5PA are snippets with arm-chair termination, *i.e.*, their π states are beaded on the graphene π-band along the $\Gamma - M$ direction. The position of the Fermi-energy with respect to the vacuum energy, defined as gap center in Fig. 2, is about the same for all three molecules and lies slightly higher than in graphene. Finally as depicted in Fig. 1e, also the disc-shaped 5DG with the chemical formula $C_{84}H_{24}$ follows the same trends regarding the difference between the GGA and the HSE functional.

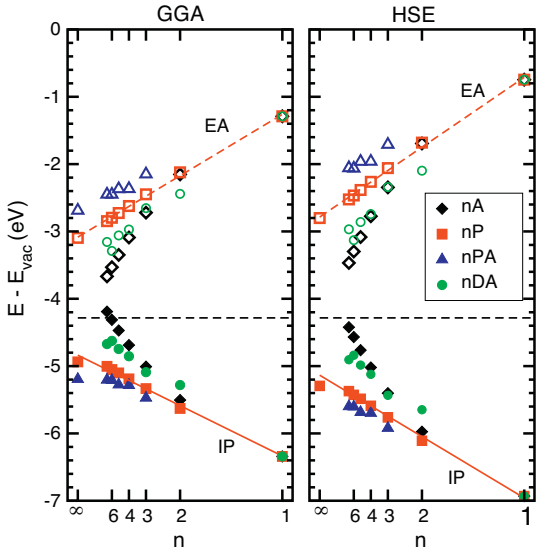

Fig. 3. Orbital energies resulting from the GGA (left panel) and HSE (right panel) for the highest occupied molecular orbital (HOMO, filled symbols) and lowest unoccupied molecular orbital (LUMO, open symbols) for the oligo-acene, oligo-phenylene, oligo-phenanthrene, and the *n*DG series. Note that a reciprocal scale has been chosen for the molecular length *n*, 1 and ∞ denoting the phenyl ring and the infinite polymer, respectively.

In order to discuss the trends with molecular length, in Fig. 3, we focus on the positions of the highest occupied molecular orbital (HOMO), *i.e.* the ionization potential (IP), and the lowest unoccupied molecular orbital (LUMO), *i.e.* the electron affinity (EA), for the molecular systems. The left panel shows the results for the GGA functional while the right panel displays the results for the HSE functional. The figure summarizes the results for all molecules as a function of the molecular length *n* for the oligo-acene (*n*A), the oligo-phenylene (*n*P), and the phenanthrene series (*n*PA), as well for various disc-shaped molecules denoted by *n*DG as depicted in Fig. 1. First we observe that, when plotted versus a reciprocal axis $\frac{1}{n}$, the HOMO and LUMO levels nicely follow a linear dependence thereby symmetrically lifting the IP level upwards and lowering the EA level when increasing the molecular length *n*. Note that for the oligo-phenylenes and the phen-anthrenes, the plot also includes the infinite chain result for poly-para-phenylene (PPP = ∞P) and the arm-chair graphene nano-ribbon 4-AGNR, respectively. In terms of the IP, the EA, and the band gap, the electronic structures of *n*P and *n*PA are quite similar as opposed to the oligo-acene series which exhibit significantly less stable HOMO and more re-active LUMO levels, and thus also smaller band gaps. As already mentioned in the previous paragraph, this behaviour can be derived from the band structure of graphene, to be discussed in the subsequent section, and is also the origin for the chemical instability of acenes longer than hexacene [40].

Comparing the two functionals GGA and HSE, we find that HSE symmetrically opens the gap throughout all molecules. For instance, GGA results in a band gap of only 5.1 eV for the benzene ring ($n = 1$), while HSE opens the gap to 6.7 eV, *i.e.* by a factor of roughly 1.3. We note that this HSE band gap is still considerably smaller than the quasi-particle gap of 10.5 eV from a *GW* calculation [71]. In a sense, the HSE functional can be viewed as incorporating a screened Coulomb interaction in the long-range which reduces the band gap [70]. However when shifted appropriately, it can be expected that the HSE valence band spectrum is a good approximation for the true, quasi-particle valence band spectrum of the materials under investigation. This assessment is strengthed by DFT results using an optimally tuned range separated hybrid functional [72,73,70].

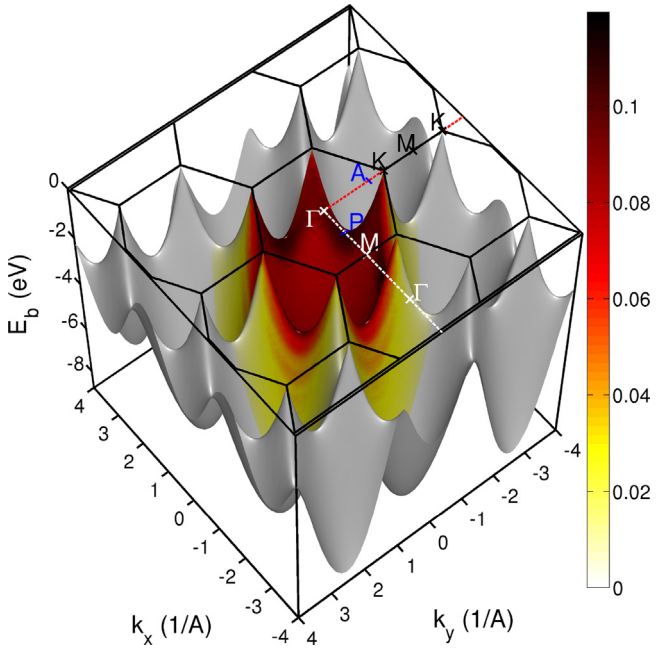

Fig. 4. Brillouin zones of graphene (honeycombs) with special points labelled in black. The red dashed lines indicate the directions for which the photoemission cross-section has been simulated. In addition, points *P* and *A* display the one-dimensional Brillouin zone boundaries of poly-para-phenylene (∞P) and poly-acene (∞A), respectively. The surface depicts the occupied π-band of graphene in an extended zone scheme, and the color code denotes the photoemission intensity with 35 eV incident photons. (For interpretation of the references to color in this figure legend, the reader is referred to the web version of the article.)

3.2. Graphene

The electronic structure of graphene has been intensively studied, both, experimentally and theoretically. In this section we first review the valence band structure of graphene, before we simulate ARPES band maps and Fermi surface maps which we compare to available experimental data from the literature.

Fig. 4 displays the π valence band of graphene as obtained from DFT using the HSE functional in an extended zone scheme over the $k_x - k_y$ plane. As already indicated in Fig. 1, our choice for the *x*-direction coincides with the arm-chair direction of graphene, while the *y*-axis has been chosen along the zig-zag direction. Correspondingly, the k_x direction is along $\Gamma - M - \Gamma$ (white dashed line), while the k_y direction is along $\Gamma - K - M - K$ (red dashed line). The π band exhibits the famous Dirac-cones at the corners of the Brillouin zone hexgaon, *i.e.* at the *K* and *K′* points, while there are saddle points at the *M* points. In addition to the high symmetry points of the graphene Brillouin zone, we have also indicated the location of two points labelled as *P* and *A* which are related to the quasi-periodic repeat units of the building blocks of the molecular systems. More precisely, *P* denotes the k_x value corresponding to the Brillouin zone boundary of the infinite PPP chain, (π/p) with $p = 4.38$ Å, and *A* denotes the k_y value corresponding to the Brillouin zone boundary of the infinite poly-acene chain, (π/a) with $a = 2.47$ Å. The color code superposed the graphene π band shown in Fig. 4 illustrates the ARPES intensity computed according to Eq. (2) when using a photon energy of 35 eV. Note, however, that here the polarization factor $|\mathbf{A}\cdot\mathbf{k}|^2$ has been omitted.

3.2.1. Band maps

In order to analyze the simulated ARPES intensity in more detail and to enable a better comparison with experimental data, we have simulated the ARPES intensity for electrons emitted along the k_y

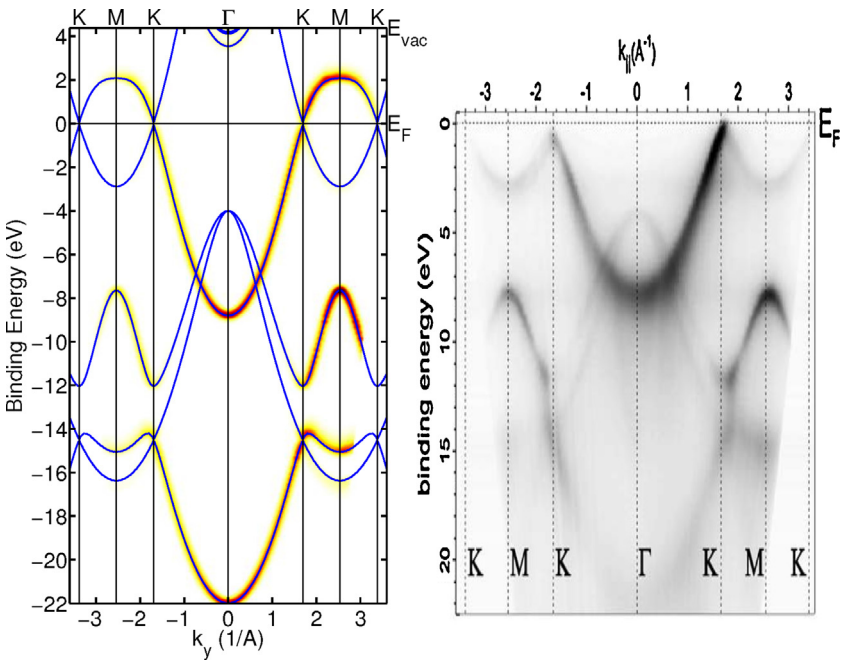

Fig. 5. Left panel: Band structure (blue lines) and simulated photoemission intensities (colormap) of graphene along the k_x direction, *i.e.*, along $\Gamma - M - \Gamma$ for 50 eV photons with in-plane polarization and 60° off-normal incidence. Right panel: experimental ARPES data of epitaxial graphene/SiC reproduced from Ref. [53]. (For interpretation of the references to color in this figure legend, the reader is referred to the web version of the article.)

and k_x directions as shown in the left panels of Figs. 5 and 6, respectively. Note that these simulations are based on the HSE electronic structure of free-standing graphene and that we have assumed 50 eV photons, an angle of incidence of 60° and light polarized in the plane of incidence and explicitly have taken into account the polarization factor $|\mathbf{A}\cdot\mathbf{k}|^2$ appearing in Eq. (2). In addition to the color coded ARPES intensity, also the band structures along the respective directions are plotted in an extended zone scheme. Note that for completeness also the ARPES intensity for initial states above the Fermi level has been included in the plots by omitting the Fermi-Dirac occupation factor in the formula.

The experimental photoelectron intensity maps shown in the right panels of Figs. 5 and 6 have been reproduced from Ref. [53] which reports ARPES intensity maps from a graphitic layer on SiC(0001) with a film thickness in the order of 2 nm. It should be noted that the photoemission data of a monolayer of graphene on SiC(0001) looks qualitatively very similar. Here, additional emissions from the SiC(0001) substrate become apparent while for a

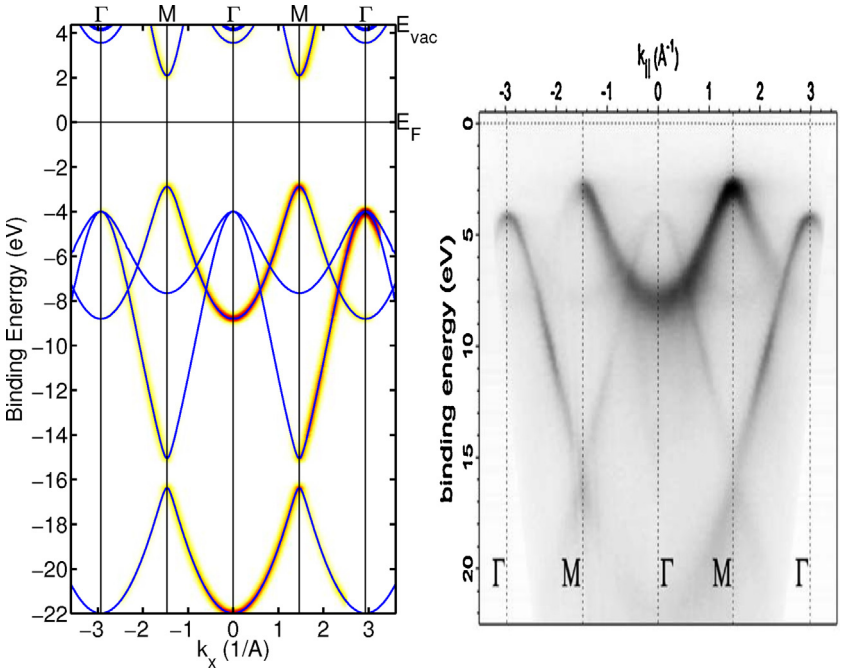

Fig. 6. Same as Fig. 5 but for the k_x-direction, *i.e.*, along $\Gamma - M - \Gamma$.

multilayer graphitic film, substrate emissions are suppressed due to the small free mean path of photoelectrons at the considered kinetic energy. The dependence of the photoemission signatures on the graphene film thickness is discussed in Ref. [54].

Starting with the k_y-azimuth along $\Gamma - K - M - K$ shown in Fig. 5, we observe an overall good agreement of the simulated and the experimental data, both in terms of the energy positions and band widths of the π and σ bands. Compared to the experimental binding energy of ≈8 eV, the bottom of the π band is slightly too deep in the simulation which lies at 8.5 eV in HSE. On the other hand, the computed energy positions of the top and bottom of the σ band are in almost perfect agreement with experiment. It should be stressed that the HSE band structure indeed leads to an improvement over the GGA band structure when assessed with the experimental data which can be seen in the DOS plots shown in Fig. 2a.

Turning to the photoemission intensities, both, the simulation and the experiment exhibits a pronounced asymmetry of the photoemission cross section with respect to positive and negative take-off angles, that is positive and negative k_y-values, respectively. This is a consequence of the polarization factor which, for light incident at 60° off normal towards the negative k_y axis has a maximum on the positive k_y side at a take-off angle of 30° that is when the emitted electron direction **k** is parallel to the vector potential of the incident light **A** (coinciding with the direction of the electric field vector). Formally, the plane wave final state approximation is expected to work only for emission directions **k** which are almost parallel to the polarization vector **A**, i.e., here corresponding to $k_y \approx +1.75\,\text{Å}^{-1}$. Nevertheless, the agreement between theory and experiment is reasonable also in a larger k_y range from roughly 0 to 3 reciprocal Angstroms corresponding to normal emission and 60° take off angle, respectively, thus deviating roughly ±30° from the $\mathbf{k} \parallel \mathbf{A}$ condition.

It is also worth noting that the valence π band leads to pronounced emissions from Γ to K with an abrupt drop in intensity from K further out towards M. Conversely, the top of the σ band is not expected to lead to significant emissions within the first BZ, but only shows strong emissions around the M point of the second BZ, while the bottom of the σ band again exhibits emissions within the first BZ, in particular at the Γ point. These intensity trends are also observed experimentally and are primarily due to the presence of the two inequivalent C atoms per unit cell. The comparison in Fig. 5 also demonstrates that the plane wave final state approximation is not only appropriate for π band but also for σ band emissions, a finding which could not be confirmed in earlier work on organic molecular layers [5]. However, it should also be mentioned that there are some deviations from the simulation results. For instance, the top of the σ band, albeit weak, is observed at normal emission (at Γ). Presumably, these differences are indeed related to a deficiency of the plane wave final state approximation which becomes more pronounced for experimental geometries strongly deviating from the $\mathbf{k} \parallel \mathbf{A}$ condition.

Regarding the k_x-azimuth along $\Gamma - M - \Gamma$ shown in Fig. 6, the agreement between simulation results and experimental data is at a similar level. For instance, the binding energy of the π saddle point at M is slightly overestimated in the HSE electronic structure compared to the experimental value. Comparing the simulated with the measured ARPES cross sections, the relative intensities of the π and σ band emissions seem to be reversed. The simulation suggests the strongest emission to arise from the σ band at the Γ point in the second BZ, while this band is observed comparably weak in experiment. On the other hand, the measurement shows the strongest emission from the π-band at the M point. Moreover, the asymmetry in the σ band emission with respect to $+k_x$ and $-k_x$ directions is not as pronounced in experiment as would be expected from the plane wave final state approximation. This suggests that plane waves may indeed approximate the final state of initial states of π symmetry better than it does for σ states. This should be the subject of further investigations.

3.2.2. Constant binding energy maps

In this section, we focus on the π-band emission of graphene. To this end, we have simulated a constant binding energy (CBE) momentum k_xk_y map at an energy of 0.7 eV below the Dirac point. The simulation results (omitting the polarization factor) for 150 eV photons are shown in panel (a) of Fig. 7, while panel (b) shows corresponding ARPES measurements (reproduced from Ref. [59]) of a single-layer graphene sample prepared on a 6H-SiC(0001) substrate. Note that on this substrate, the Fermi level is not at the Dirac point but located 0.5 eV above in the upper Dirac cone due to natural electron doping for graphene grown on SiC. Thus the experimental data shown in Fig. 7b corresponds to a binding energy of 1.2 eV below the Fermi level, that is 0.7 eV below the Dirac point in accordance with the energy position used for the simulation.

Both, in the simulation and experiment, one observes emission pockets from the Dirac cones around each K and K' points located at the corners of the hexagons. Ideally, the pockets should be circles but are warped to be rounded triangles due to the deviations from the linear dispersion relation owing to second-nearest-neighbour hopping [74]. Also, the intensity distribution of each pocket is not uniform, but varies strongly when moving around a K or K' point. This variation is known to be due to the difference in the phases of the two p_z orbitals of the inequivalent carbon atoms in the unit cell. This phase difference also plays the role of the pseudospin in forming the Dirac cone dispersion as discussed, for instance, in Ref. [59]. The agreement between the simulation and experiment is remarkable demonstrating that a plane wave represents an excellent approximation for the final state of the photoemission process from the graphene π bands. As already demonstrated for graphene [59] and for various π-conjugated molecules, including sexiphenyl (6P) [4] and pentacene (5A) [25], this indeed opens the possibility to reconstruct real space orbital densities from multiple BZ ARPES data.

3.3. Oligo-phenylenes

As can be seen from Fig. 1, oligo-phenylenes (nP) may be viewed as graphene snippets cut out along the armchair direction (x), or in other words may be termed finite length armchair graphene nanoribbons (AGNR) with the least possible lateral extension. In the gas phase, however, oligo-phenylenes are known to exhibit an inter-ring torsion between adjacent phenyl rings [75,76]. This torsion is a consequence of the electro-static repulsion of hydrogen atoms on neighboring rings. The application of pressure [77,78] or the adsorption on moderately strongly interacting substrates may planarize the molecules [14]. Since here we are interested in the electronic structure of oligo-phenylenes as observed by ARPES from highly oriented films, we restrict ourselves to planar nP molecules. Moreover, the comparison with graphene's electronic structure discussed in the previous section becomes more evident when studying planar nP molecules. Effects arising from inter-ring torsion angles are discussed in a separate publication [65]. Here, we focus on the technologically most relevant 6P (sexi-phenyl).

3.3.1. Band maps

Sexi-phenyl consists of six phenyl rings linked together in the para-position. Thus, it has a total of 36 carbon atoms each contributing one electron to the π electronic orbitals, 18 of which are occupied [76]. Inspection of a simulated ARPES band map over the entire valence band range given in the top panel of Fig. 8 clearly reveals the similarities with the parent compound graphene. Comparing with Fig. 6, we observe that 12 out of the 18 valence π orbitals are threaded as beads along the graphene π band in $\Gamma - M$ direction

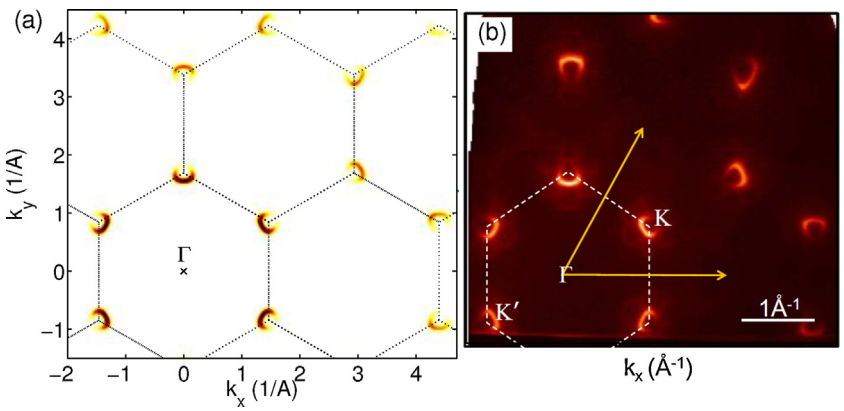

Fig. 7. (a) Simulation of a constant binding energy ARPES map of graphene 0.7 eV below the Dirac point with a photon energy of 150 eV. (b) Corresponding experimental data reproduced from Ref. [59].

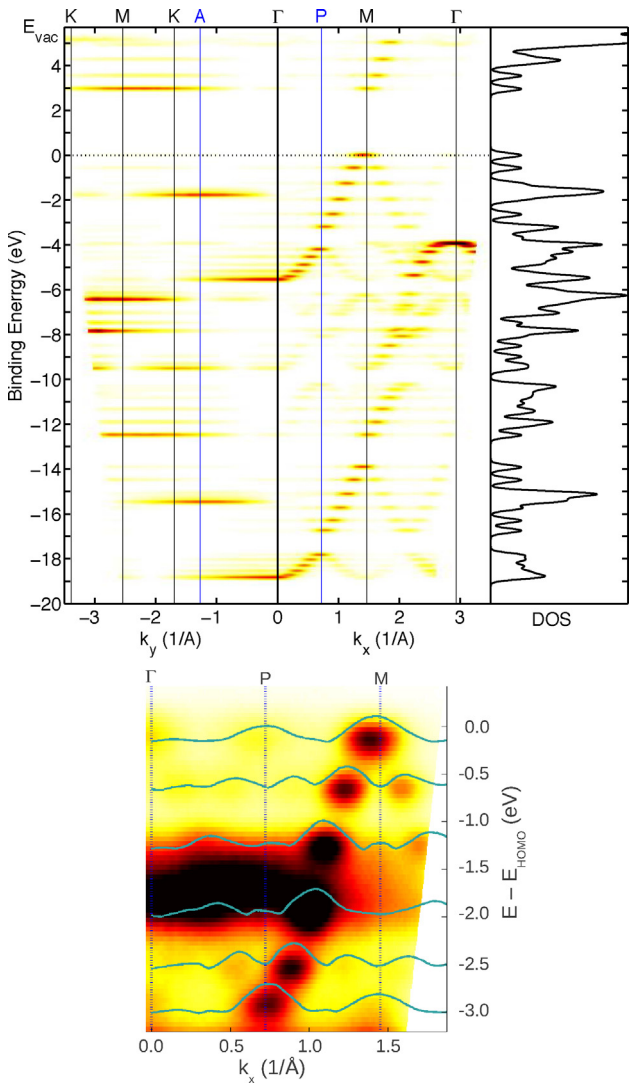

Fig. 8. Top: Simulated ARPES band map of sexiphenyl (6P) using 50 eV photons along k_x (from Γ to the right) and k_y (from Γ to the left). In addition, the density of states is also shown. For a better comparison, the Brillouin zone boundaries of graphene (vertical black lines) and of the infinite polymer chain (blue lines) are shown. Bottom: Experimental ARPES of a 6P multilayer film along the molecular axis with 21.2 eV photons [3]. (For interpretation of the references to color in this figure legend, the reader is referred to the web version of the article.)

from −5.5 eV up to the HOMO energy (set to zero energy) forming the so-called "bonding" band. The k_x-width of these emissions is inversely proportional to the length of the molecule which can be nicely seen when comparing the corresponding band maps for the shorter oligo-phenylenes. The remaining six π orbitals of 6P form the so-called "non-bonding" orbitals [76,3]. Due to a nodal plane along the *x*-direction, they are not visible along k_x but only along the k_y direction, and they give rise to the pronounced peak in the DOS slightly above −2 eV binding energy. Note that a small interring torsion angle and/or a tilt angle of the molecular plane with respect to the substrate's surface would lift the symmetry restrictions and make the non-bondings also observable along the molecular axis [3,65]. The "intra-molecular" band dispersion in sexiphenyl could already been measured for the upper 6 bonding orbitals for a multilayer film [3], reproduced in the bottom panel of Fig. 8, as well as for monolayer films adsorbed on Cu(1 1 0) [14] and Al(1 1 0) [65].

Perpendicular to the long molecular axis, *i.e.* along the k_y direction, the orbitals belonging to the "bonding" band are not observable except for the lowest lying one which has no nodal plane along k_y. Their k_y width is inversely proportional to the short molecular axis, thus of the order of the $\Gamma - A$ distance.

Also the σ valence electronic structure of 6P nicely resembles the σ bands of graphene in $\Gamma - M$ direction (compare Fig. 6). Starting from the bottom of the intra-molecular σ band at Γ, there are 6 orbitals threaded on the graphene band within each BZ of PPP with small gaps appearing at the corresponding BZ boundaries *P*. Compared to graphene, the relative positions of the σ and π bands is different owing to the significantly increased inter-ring C—C bond in 6P which de-stabilizes its π-band compared to the graphene counterpart. It should be noted that the intra-molecular dispersion of the σ bands in 6P has not yet been observed presumably because too low photon energies have been used in experiments conducted so far. It would be desirable to perform such ARPES experiments using larger photon which could reveal the relative positions of π and σ states which would represent a stringent benchmark for electronic structure methods.

3.3.2. Momentum maps

In this section we compare simulated CBE k_xk_y maps of selected 6P orbitals with corresponding emission patterns from graphene. Panels (a) and (b) of Fig. 9 display momentum maps of graphene calculated at the binding energy of the π band saddle point (*M*-point) and 0.5 eV below it, respectively, assuming 150 eV photons. Panels (c) and (d) depict the corresponding simulations of the 6P HOMO and HOMO-1 orbitals. Several similarities as well as differences can be noticed. The positions as well as the intensities of the molecular features along the k_x direction can be well-understood in terms of the respective emission features of graphene. Clearly,

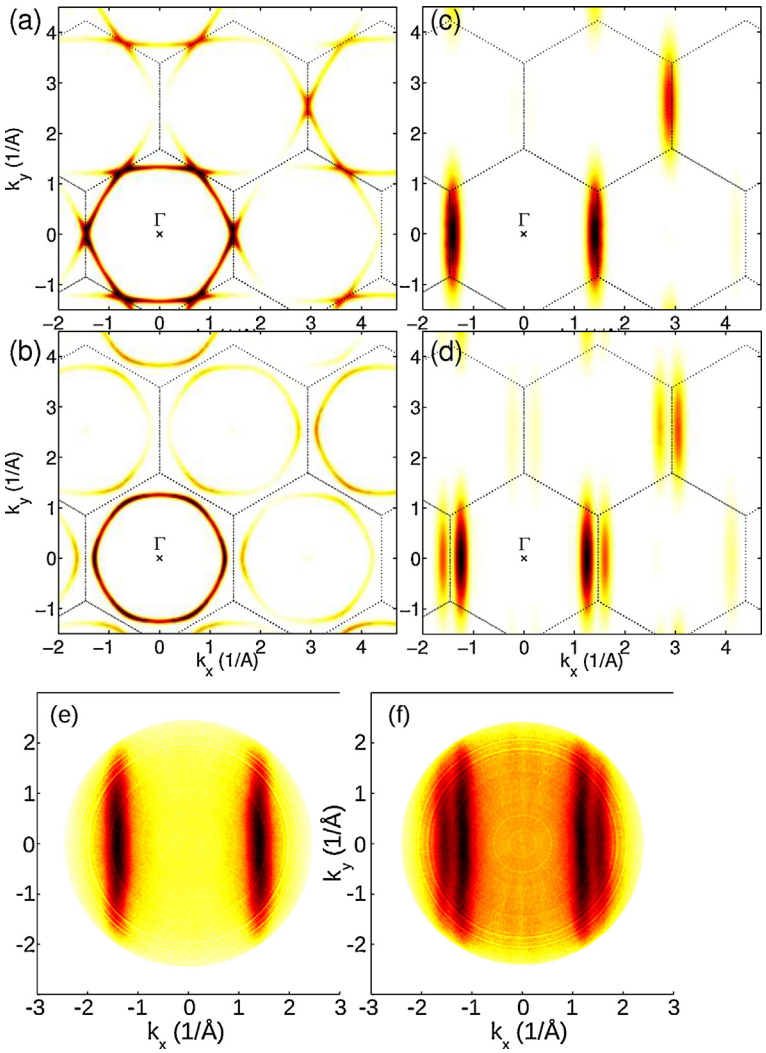

Fig. 9. Panels (a) and (b) show simulated constant binding energy ARPES maps of graphene at the saddle point of the π band (M-point) and 0.5 eV below it, respectively, for 150 eV photons. Panels (c) and (d) are simulated momentum maps of the 6P HOMO and HOMO-1, respectively. Panels (e) and (f) are experimental momentum maps of the 6P HOMO and HOMO-1, respectively, as measured on a 6P monolayer on Al(110) using 35 eV photons [65].

and as already mentioned in the previous section, the k_x-width of the HOMO and HOMO-1 emissions is a result of the finite length of the molecule. Note that the finite width of the graphene feature is only due to an artificial k-space broadening of 0.03 Å^{-1} which had to be applied for numerical reasons. Due to the short length of the 6P molecule in y-direction, the molecular features are greatly extended in k_y direction.

The simulated momentum maps of the 6P HOMO and HOMO-1 in panels (c) and (d) of Fig. 9 are also compared to corresponding measurements depicted in panels (e) and (f), respectively. Note that 6P momentum maps of the HOMO and the LUMO for a monolayer of 6P on Cu(1 1 0) could already be measured by ARPES in accordance with our electronic structure calculations [4]. Furthermore, a 6P monolayer doped with Cs could also reveal the momentum structure of the LUMO and LUMO+1 orbitals in agreement with theory [24]. Here, we reproduce ARPES data measured for a monolayer of 6P/Al(1 1 0) from Ref. [65]. Both, the CBE maps at the binding energy of the HOMO (e) and HOMO-1 (f) reflect the characteristic patterns predicted by the simulations, most notably, the splitting of the main lobe into two features centered around the M point for the HOMO-1. However, the experimental width of the lobes along the k_y direction appears to be somewhat increased compared to the simulation. This may be due to a not perfectly flat adsorption geometry of the 6P monolayer on Al(1 1 0). Concerning future experiments, it would also be interesting to investigate whether the larger $k_\parallel$ features predicted by the simulations can indeed be measured when performing the experiments with a larger photon energy.

3.4. Oligo-acenes

As opposed to oligo-phenylenes, oligo-acenes can be viewed as snippets cut out from graphene along the *zig-zag* direction (y), or in other words they may be termed finite length zig-zag graphene nanoribbons with the least possible lateral extension. More traditionally, the linear acenes are characterized as polycyclic aromatic hydrocarbons consisting of n linearly-fused benzene rings (Fig. 1). Here, we focus on the technologically most relevant 5A (pentacene). It should be noted that the actual synthesis of longer acenes ($n > 5$) still remains as a challenging task for synthetic chemists. The major challenges of preparing longer acenes include their poor stability at room temperature, especially in solution, and their poor solubility which hampers detailed experimental characterization [40].

3.4.1. Band maps

Pentacene consists of five linearly fused phenyl rings, thus having 22 carbon atoms where each carbon atom contributes one

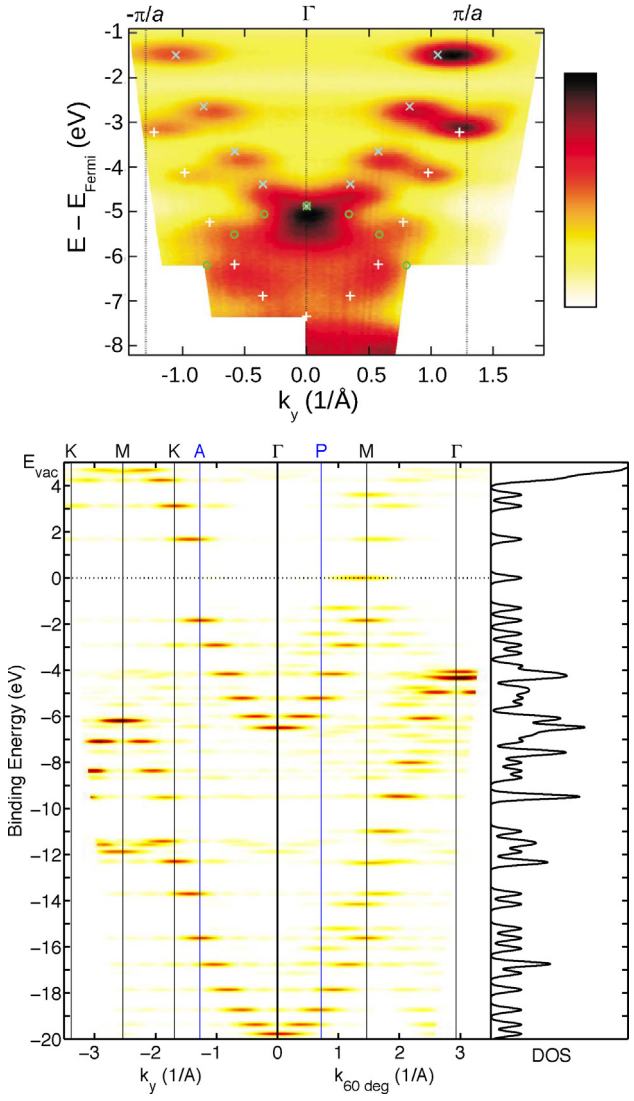

Fig. 10. Top: Experimental ARPES band map of a multilayer pentacene film along the long molecular axis (y-direction) using 21.2 eV photons as reproduced from Ref. [46]. Bottom: Simulated ARPES band map of pentacene (5A) using 50 eV photons along a direction 60° rotated from k_x (from Γ to the right) and k_y (from Γ to the left). In addition, the density of states is also shown. For a better comparison, the Brillouin zone boundaries of graphene (vertical black lines) and of the infinite polymer chain (blue lines) are shown. (For interpretation of the references to color in this figure legend, the reader is referred to the web version of the article.)

electron to the π electron system, 11 orbitals of which are occupied. As already discussed in a previous publication [46], these π orbitals can be further grouped into a "lower" and an "upper" intramolecular π band comprising 6 and 5 orbitals, respectively. ARPES data of a highly oriented multi-layer of pentacene nicely demonstrates these two π orbital bands of pentacene as shown in the top panel of Fig. 10 (reproduced from Ref. [46]). Here, the cyan crosses (white plus signs) indicate the energy and major k_y positions of the orbital emissions belonging to the upper (lower) band as obtained from a GGA-DFT calculation while the color-map represents the measured photo-emission intensity. The green circles indicate the energy positions of the topmost σ orbitals which are, however, expected to be seen only at larger $k_{\|}$ values. With respect to 6P, we observe that all molecular emissions have a broader k-range. This is a direct consequence of the much shorter molecular length of pentacene (≈14 Å) which is only about half the length of sexiphenyl (≈26 Å). Comparing the simulated with the measured k_y positions of the orbital emissions, we observe a good agreement for the lower π band, while the measured k_y positions are somewhat larger than the simulated ones for the upper π band. This effect has been explained by intermolecular interactions which lead to a spatial compression of orbitals which could be nicely shown by comparing simulations for the isolated 5A molecule with calculations for a 5A bulk structure [48].

The bottom panel of Fig. 10 shows an ARPES simulation for an isolated 5A molecule over its entire valence band energy range. Here, the six emissions from the lower band can be clearly observed in the k_y direction starting from Γ at a binding energy of −6.5 eV following the graphene π band dispersion along the $\Gamma - K$. The emission from the upper π band can neither be observed in the k_y (parallel to the long molecular axis) nor in the k_x direction (perpendicular to the molecular axis) due to nodal planes in these directions (see Refs. [46,25] for respective orbital images). Therefore in the bottom panel of Fig. 10, we have simulated an ARPES band map at an angle of 60° from the x-axis which corresponds to another $\Gamma - M$ direction of graphene. Here, both the upper and the lower π bands can be observed although the upper one with smaller intensity. The reason why both bands can be experimentally observed in k_y direction (top panel of Fig. 10) is that in the multilayer pentacene film, the molecules are tilted but still retain a uniaxial alignment [46].

As mentioned earlier, the highest occupied state of the lower π band is in fact the HOMO-2 centred at the A point at a binding energy slightly above −2 eV. Also the LUMO and LUMO+1 of pentacene belong to this "band" and are located at k_y values around the K point of graphene. In contrast to 6P and owing to the zig-zag termination of 5A, the "lower" intra-molecular π band including the HOMO-2 on the occupied side and the LUMO and LUMO+1 at the unoccupied side of the spectrum can be viewed as the finite-molecule version of the Dirac-cone dispersion of graphene in zig-zag direction.

3.4.2. Momentum maps

This point of view can be further illustrated by comparing CBE maps of graphene and pentacene at appropriate energies as discussed in this subsection. Panels (a) and (b) of Fig. 11 display constant binding energy ARPES simulations (150 eV photons) for graphene 0.5 eV above and 0.7 eV below the Dirac point, respectively. Note that the data shown in (b) is identical to the one already depicted in Fig. 7 and is repeated here to enable a better comparison with pentacene. To this end, panels (c) and (d) show simulated momentum maps (for 150 eV photons) for the pentacene LUMO+1 and LUMO. Clearly, pentacene is a linear, rod-like molecular and therefore cannot be expected to exhibit the sixfold symmetric momentum pattern observed for graphene. Rather it is characterized by broad lobes slightly inside (outside) the first K point in k_y direction for the LUMO (LUMO+1) resembling the circular pockets around the K points in graphene. As already mentioned above, the width of these lobes in k_y (k_x) direction is inversely proportional to the length of the molecule along the long (short) molecular axis. There are additional side lobes owing to the finite lateral size of the acenes which are discussed in more detail in Ref. [12].

As panels (e) and (f) of Fig. 11 show, experimental ARUPS momentum maps of a monolayer of 5A on Cu(1 1 0) and Ag(1 1 0), respectively, compare well with a simulated LUMO map for isolated 5A molecule [12]. Thus, on both substrates, there is charge transfer from the metal into the LUMO of 5A, while the LUMO+1 remains unoccupied and can therefore not be observed with ARPES. It should also be noted that the long molecular axis of 5A is oriented parallel (perpendicular) to the [1-10] direction on Cu(1 1 0) (Ag(1 1 0)) which can be directly inferred from the ARPES maps. When analyzing the measured momentum maps of the filled LUMO in more detail one finds that on Ag(1 1 0), it remains essentially

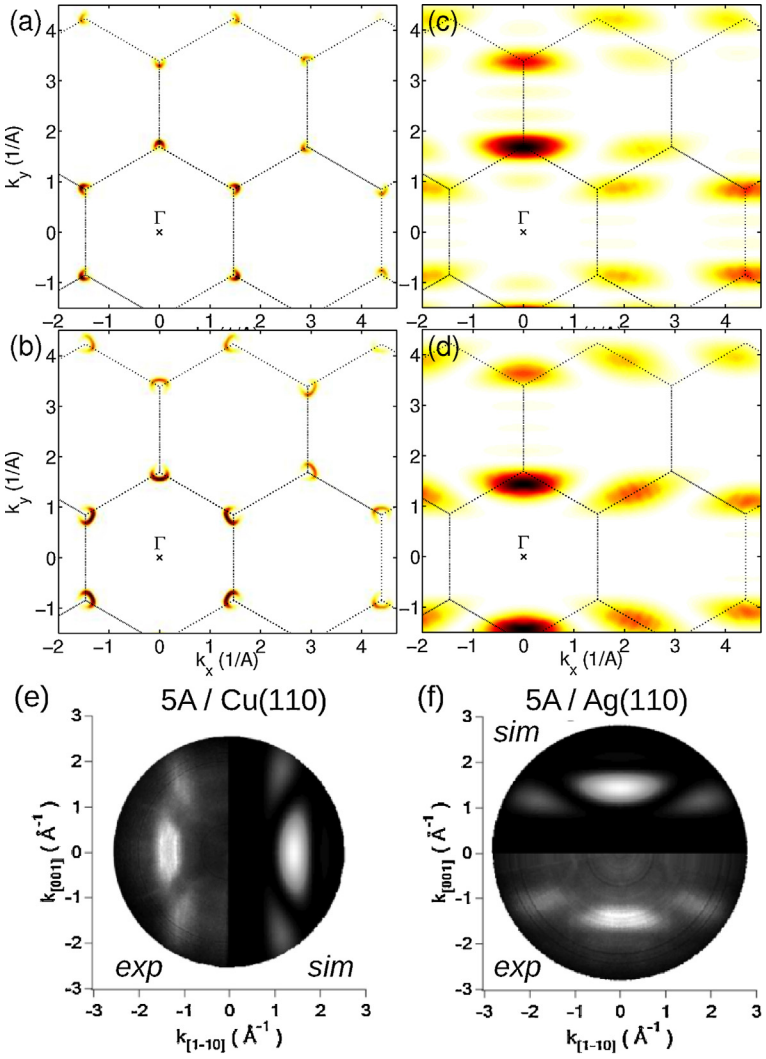

Fig. 11. Panels (a) and (b) show simulated constant binding energy ARPES maps of graphene 0.5 eV above and 0.7 eV below the Dirac point, respectively, for 150 eV photons. Panels (c) and (d) are corresponding simulated momentum maps of the 5A LUMO+1 and LUMO, respectively. Finally, panels (e) and (f) compare experimental ARUPS momentum maps (*exp*) of a monolayer of 5A on Cu(1 1 0) and Ag(1 1 0), respectively, with a simulated LUMO map for isolated 5A molecule (*sim*) [12]. Note that the long molecular axis of 5A is oriented parallel (perpendicular) to the [1-10] direction on Cu(1 1 0) (Ag(1 1 0)).

isolated-molecule-like, while a pronounced substrate-enhanced dispersion and an orbital modification are observed upon adsorption on Cu(1 1 0) [12].

3.5. Phen-anthrenes

The three-ring molecule (3PA, Fig. 1) may be viewed as composite of phenyl and anthracene which leads to its conventional name phenanthrene ($C_{14}H_{10}$). The next molecule in the series (4PA) is chrysene with the chemical formula $C_{18}H_{12}$, thus it is an isomer of tetracene. In contrast to tetracene, chrysene is colorless owing to its much larger band gap (compare Fig. 3). In fact the electronic structure of the whole phenanthrene series *n*PA is more closely related to the oligo-phenylenes rather than the oligo-acenes. This can already be explained with the empirical π-sextet rule of Clar [31].

Here we focus on the five-ring member picene (5PA), which is an isomer of pentacene with the chemical formula $C_{22}H_{14}$, and is probably the most prominent representative of the phenanthrene series. It has attracted considerable attention as a new candidate for an organic device material because of its high stability against oxidation, high mobility ($3\,cm^2\,V^{-1}\,s^{-1}$) and superconducting properties ($T_c \approx 20\,K$) when doped with potassium [79]. Recently, the band structure of picene single crystals has been investigated by UPS [49], and the impact of molecular orbital distribution on the photoelectron intensity for a picene film has been discussed for a number of occupied molecular orbitals of picene [11].

The left column of Fig. 12 shows simulated momentum maps of the picene HOMO and HOMO-1 which are, according to the HSE calculation for an isolated molecule, only 0.28 eV apart. The symmetries of the emissions patterns are, however, distinctly different. While the HOMO is expected to show no emission along the k_x direction and the strongest emission along k_y, the opposite is true for the HOMO-1. Moreover, when concentrating on the emission along these principal directions as a function of take-off angle, as indicated by the blue lines in the maps, one expects a broad feature for the HOMO while a sharper peak is predicted for the HOMO-1. This is indeed observed experimentally as is shown by take-off angle dependence of the photoemission intensity depicted in the right column of Fig. 12 as reproduced from Ref. [11]. It should also be noted that the simulation results presented in this Ref. [11], which are based on a multiple-scattering theory, turn out to be very similar to the simulations obtained in this work based on the plane

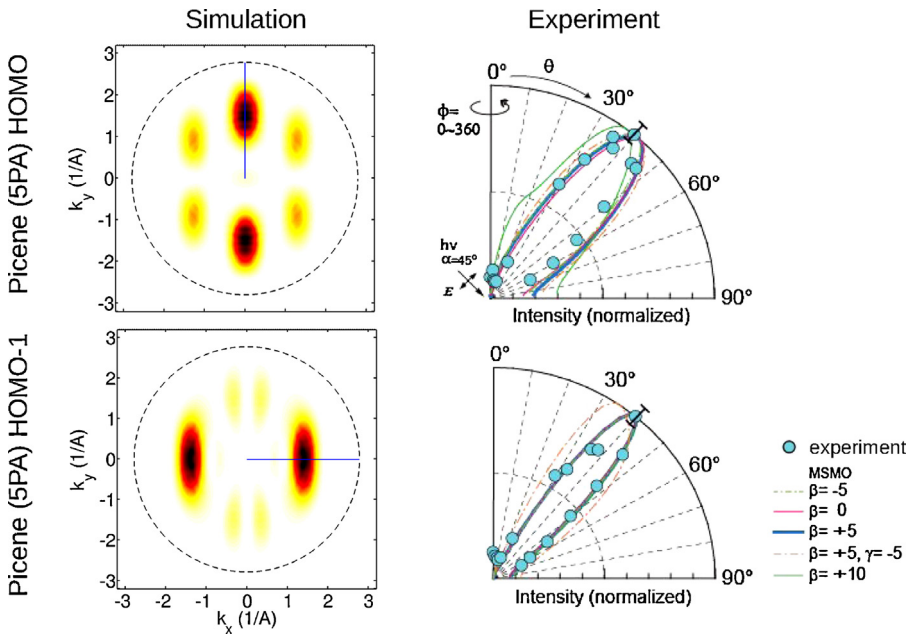

Fig. 12. Simulated momentum maps of the picene HOMO and HOMO-1 (left column) compared to the experimental polar angle dependence as taken from Liu et al. [11].

wave approximation. This demonstrates that also for this system, scattering effects do not alter the emission patterns significantly.

In Fig. 13, we present ARPES simulations for picene (5PA) comprising the complete valence electronic structure as a band map along the k_x and k_y directions. Focusing first on the HOMO and HOMO-1 orbitals again, we recognize their already discussed properties. The HOMO appears as a broad feature along k_y, while the HOMO-1 turns up as a sharper peak along k_x. In fact these widths reflect the inverse dimensions of the molecule in y and x direction, respectively. Moving down in energy along the k_x-direction, one can clearly reveal the similarities of picene with the oligo-phenylenes, more precisely with terphenyl (3P). Picene's orbitals appear threaded as beads along the graphene π band in $\Gamma - M$ direction from about −5.7 eV up to the HOMO-1.

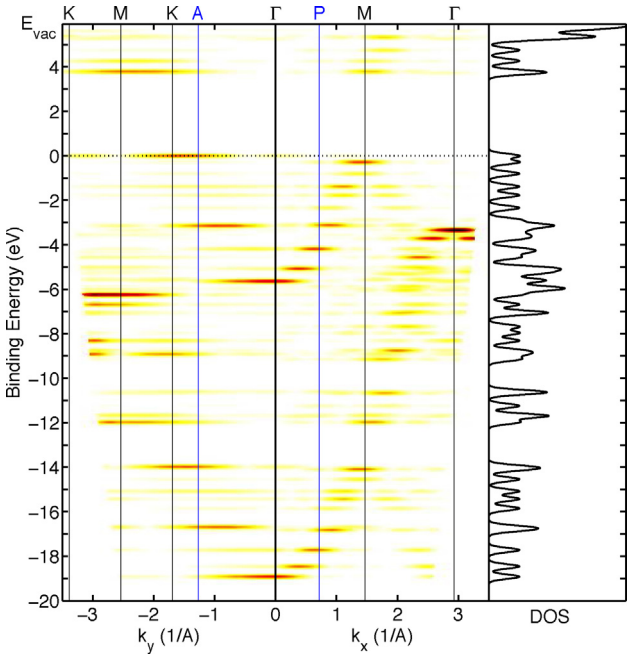

Fig. 13. Simulated ARPES band map of picene (5PA) using 50 eV photons along k_x (from Γ to the right) and k_y (from Γ to the left). In addition, the density of states is also shown. For a better comparison, the Brillouin zone boundaries of graphene (vertical black lines) and of the infinite polymer chain (blue lines) are shown. (For interpretation of the references to color in this figure legend, the reader is referred to the web version of the article.)

3.6. Disc-shaped nano graphene

Finally in this section, we present ARPES simulation results for disc-shaped PAHs which we term *n*DG (inferred from the word disc-shaped nano-graphenes) where n is a measure for the number of rings across the diameter of the molecule. In particular, we concentrate on two representatives, namely coronene (2DG, $C_{24}H_{12}$) and 5DG ($C_{84}H_{24}$) which are depicted in Fig. 1. Both molecules are of approximate circular shape and their dimensions in x and y direction are comparable to biphenyl (2P) and anthracene (3A) in the case of coronene, while 5DG's extent along x and y is equivalent to quater-phenyl (4P) and hexacene (6A), respectively.

3.6.1. Band maps

In Fig. 14, we compare a simulated band map for an isolated coronene molecule (a) with a measured ARPES band map for coronene adsorbed on Ag(111) (b) along the k_y direction. Superimposed in both panels is the graphene band structure (red dashed lines) which has been shifted in energy such that the bottom of the π band of graphene coincides with the lowest lying π orbital of coronene. The energy zero is set to the HOMO of coronene. As already observed for the other PAHs discussed previously, the molecular emission features are centered around the corresponding graphene bands. When comparing the experimental data with the simulation, several emissions can be unambiguously identified, three of which, at energies 0.0 eV (the HOMO), −1.2 eV and −6.0 eV, have been discussed in detail in Ref. [8] where they have been denoted MO1, MO2, and MO3, respectively. Note that between 1.5 and 5.5 eV below the HOMO, the emissions are dominated by Ag d-states, which prevents a definite assignment of emission patterns to specific molecular states in this energy range. It is worth noting, however, that below the Ag-d band, several emission features are visible in the experimental map which can be attributed to σ

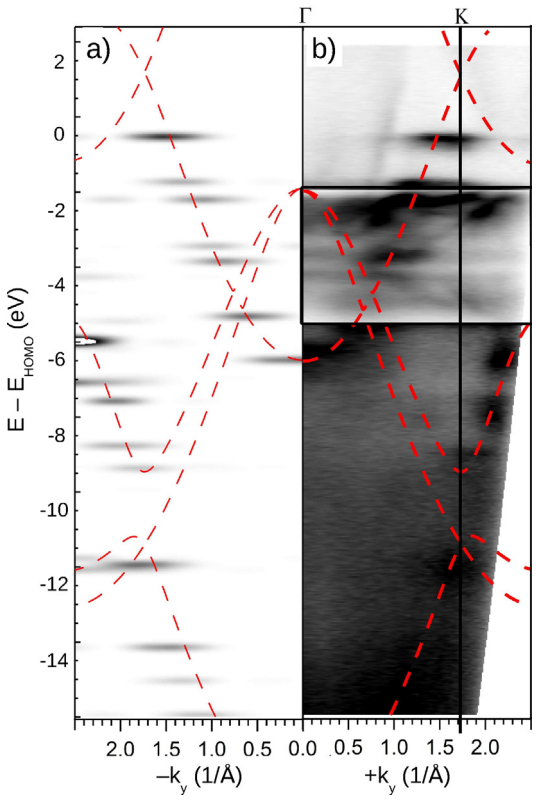

Fig. 14. Simulated (a) and measured (b) band map for coronene (2DG) along the k_y direction. For comparison, the red dashed lines represent the calculated band structure of graphene. The measurement [8] is performed for a monolayer of coronene/Ag(111) using He-II radiation (40.8 eV). Note that the intensity scale in the Ag d-band region (black rectangle) has been re-scaled. (For interpretation of the references to color in this figure legend, the reader is referred to the web version of the article.)

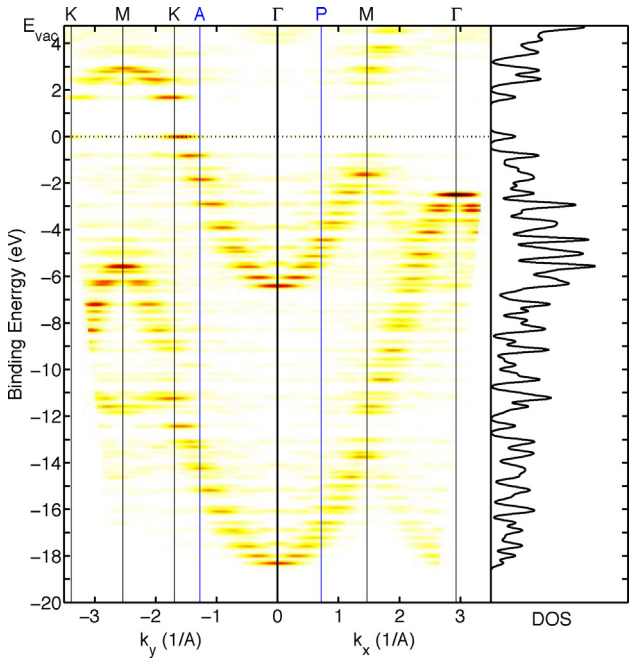

Fig. 15. Simulated ARPES band map of 5DG using 50 eV photons along k_x (from Γ to the right) and k_y (from Γ to the left). In addition, the density of states is also shown. For a better comparison, the Brillouin zone boundaries of graphene (vertical black lines) and of the infinite polymer chain (blue lines) are shown. (For interpretation of the references to color in this figure legend, the reader is referred to the web version of the article.)

orbitals of coronene. Note that similar results could also be obtained for hexa-benzo-coronene (3DG) which are reported in Ref. [8].

We now move on to the larger 5DG molecule. Fig. 15 displays a simulated ARPES band map of 5DG ($C_{84}H_{24}$) along the k_x and k_y directions based on 50 eV photons. Note that in contrast to all other band maps shown previously, this simulation is based on GGA results rather than the hybrid functional HSE due to computational limitations. The main difference between GGA and HSE results have already been summarized in Sec. 3.1. For instance, the 5DG molecule has a GGA band gap of 1.68 eV which is somewhat increased to 2.12 eV when using the range-separated hybrid functional HSE. Also, the total π and σ band widths are increased when going from a semi-local to the hybrid functional. It should be stressed, however, that the angular patterns of simulated ARPES intensities are hardly affected by the choice of the functional. This is due to the fact that the orbital shapes are less sensitive to the choice of exchange-correlation functional than the orbital energies [5].

From what was said above, we expect the intra-molecular band structure of 5DG along k_x and k_y to resemble the band structures of 4P and 6A, respectively. The valence band maps of 5DG, both, along the $\Gamma - M$ and $\Gamma - K$ directions clearly resemble those of graphene (compare Figs. 6 and 5). Given the fact that the k_y distribution of the HOMO of 5DG seen at $E_b = 0$ eV is centred slightly inside the K point, it should be compared to a graphene state somewhat below the Dirac point. Similarly, the 5DG LUMO corresponds to a graphene state slightly above the Dirac cone as exemplified by its k_y maximum a little outside the K point. Looking along $\Gamma - M$, we also observe that the top of the π band ($E_b \approx -1.7$ eV) is located slightly inside the M point. This is due to a finite size effect. In contrast to the infinite graphene, the wave function of this state is able to extend somewhat beyond the edges of the molecule thereby increasing the spatial wave length of the orbital. Moreover, we can also anticipate that the electronic structure of such disc-shaped nano-graphene will in fact be closest to that of the infinite graphene sheet. We will demonstrate this statement by comparing constant binding energy momentum maps of the 5DG HOMO with corresponding ARPES simulations for graphene.

3.6.2. Momentum maps

CBE momentum maps of coronene (2DG) and hexa-benzo-coronene (3DG) have already been simulated and compared to experimental ARPES maps in Ref. [8]. There, for each molecule three different molecular states of the adsorbed monolayers of 2DG and 3DG on Ag(1 1 1) could be identified. Here, we focus on the simulation of CBE maps for the larger 5DG molecule for which currently no experimental data is available.

In Fig. 16, we investigate the close connection between the spatial structure of the 5DG orbitals and the corresponding states in graphene which becomes evident by simulating ARPES momentum map for graphene and 5DG at appropriate binding energies. While panels (a) and (b) show simulations of ARPES k_xk_y maps of graphene, namely 0.7 eV below the Dirac point and at the M saddle point, respectively, panels (c) and (d) display the simulated CBE emission patterns of the 5DG HOMO and of the state 1.7 eV below the HOMO energy, respectively. In contrast to the momentum maps for the linear, rod-like molecules 6P and 5A, the momentum maps of 5DG are six-fold symmetric in the same way as the graphene maps. The intensity patterns, both with respect to their positions in the k_x and k_y plane and their relative intensities, nicely resemble the corresponding momentum maps of graphene. The obvious difference between graphene and the molecular system 5DG clearly is the k-width of the feature in the momentum maps. As already mentioned above, this width is inversely proportional to the spatial extent of

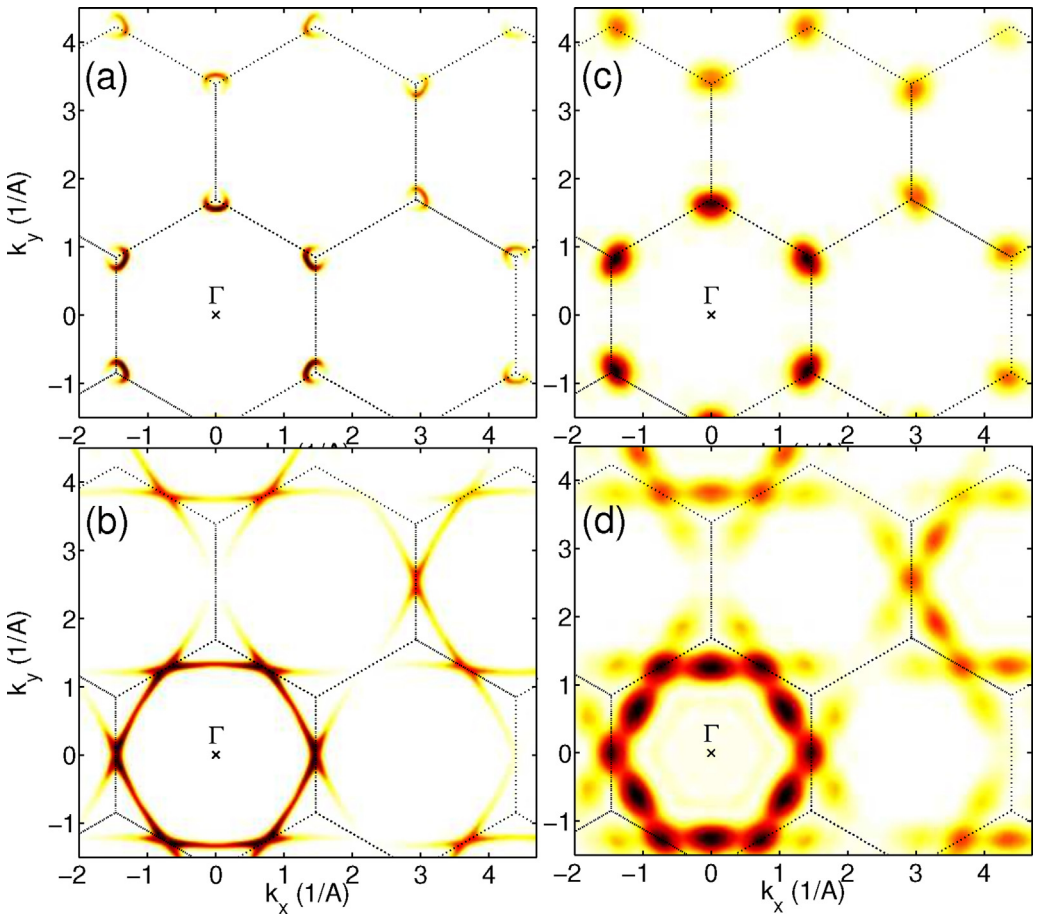

Fig. 16. Panels (a) and (b) show simulated constant binding energy ARPES maps of graphene 0.7 eV below the Dirac point and at the *M* saddle point, respectively, for 150 eV photons. Panels (c) and (d) are simulated momentum maps of the corresponding energies for 5DG, that is for the HOMO and 1.7 eV below the HOMO energy, respectively.

the molecule which is ≈15 Å in the case of 5DG in both *x* and *y* directions. More precisely, we can expect a FWHM of $\approx(2\pi/15) \approx 0.4$ Å^{-1} in this example. Note that for the infinite graphene and neglecting lifetime effects, as we do in our approach, the width would be in principle infinitesimal small. However, for technical reasons we have included an artificial broadening of 0.035 Å^{-1} in our simulations. In other words, this corresponds to a coherence length of ≈180 Å in the case of graphene.

4. Conclusions and perspectives

We have presented a comprehensive computational study on the angle-resolved photoemission of polycyclic aromatic hydrocarbons (PAHs). The oligo-phenylenes, the oligo-acenes, the phenanthrene series, a number of disc-shaped molecules as well as free-standing graphene have been treated (an overview over the investigated systems is provided in Fig. 1). We have found that the range-separated hybrid functional according to Heyd, Scuseria, and Ernzerhof (HSE) [64] provides an excellent description of all systems under study and represents a significant improvement over semi-local GGA functionals. This regards the valence band widths of π and σ states and also their relative energy alignment when compared with experimental photoemission data.

The simulations of the angle and binding-energy dependent photocurrent are based on the one-step model of photoemission under the assumption of a plane wave for the final state. It is shown that this approach, sometimes called orbital tomography, not only works for molecules such as sexi-phenyl or pentacene, but the theoretical description can be straight-forwardly extended to two-dimensionally periodic systems exhibiting strong energy dispersion. The simulated band maps and constant binding energy momentum maps of graphene turn out to be in excellent agreement with experimental findings from the literature. This opens the possibility to experimentally determine Wannier functions of graphene from ARPES data by making use of the relation between the ARPES intensity and the Fourier transform of the wave function of the emitting state. Moreover, the phase problem which one encounters when reconstructing wave functions from ARPES data could be tackled with a procedure similar to molecular systems [25], for instance, by constructing maximally localized Wannier functions [80,81]. This will be a highly interesting topic for future studies.

Acknowledgement

We acknowledge financial support from the Austrian Science Fund (FWF) projects P23190-N16 and P27649-N20.

Appendix A. Supplementary Data

Supplementary data associated with this article can be found, in the online version, at http://dx.doi.org/10.1016/j.elspec.2015.06.003

References

[1] J.W. Gadzuk, Surface molecules and chemisorption. II Photoemission angular distributions, Phys. Rev. B 10 (1974) 5030–5044, http://dx.doi.org/10.1103/PhysRevB.10.5030

[2] S. Kera, S. Tanaka, H. Yamane, D. Yoshimura, K. Okudaira, K. Seki, N. Ueno, Quantitative analysis of photoelectron angular distribution of single-domain organic monolayer film: Ntcda on ges(001), Chem. Phys. 325 (2006) 113–120, http://dx.doi.org/10.1016/j.chemphys.2005.10.023

[3] G. Koller, S. Berkebile, M. Oehzelt, P. Puschnig, C. Ambrosch-Draxl, F.P. Netzer, M.G. Ramsey, Intra- and intermolecular band dispersion in an organic crystal, Science 317 (2007) 351, http://dx.doi.org/10.1126/science.1143239

[4] P. Puschnig, S. Berkebile, A.J. Fleming, G. Koller, K. Emtsev, T. Seyller, J.D. Riley, C. Ambrosch-Draxl, F.P. Netzer, M.G. Ramsey, Reconstruction of molecular orbital densities from photoemission data, Science 326 (2009) 702–706, http://dx.doi.org/10.1126/science.1176105

[5] P. Puschnig, E.-M. Reinisch, T. Ules, G. Koller, S. Soubatch, M. Ostler, L. Romaner, F.S. Tautz, C. Ambrosch-Draxl, M.G. Ramsey, Orbital tomography: deconvoluting photoemission spectra of organic molecules, Phys. Rev. B 84 (2011) 235427, http://dx.doi.org/10.1103/PhysRevB.84.235427

[6] A.M. Bradshaw, D.P. Woodruff, Molecular orbital tomography for adsorbed molecules: is a correct description of the final state really unimportant? New J. Phys. 17 (2015) 013033, http://dx.doi.org/10.1088/1367-2630/17/1/013033

[7] B. Stadtmüller, M. Willenbockel, E. Reinisch, T. Ules, M. Ostler, F. Bocquet, S. Soubatch, P. Puschnig, G. Koller, M.G. Ramsey, F.S. Tautz, C. Kumpf, Orbital tomography for highly symmetric adsorbate systems, Eur. Phys. Lett. 100 (2012) 26008, http://dx.doi.org/10.1209/0295-5075/100/26008

[8] M. Wießner, N. Rodriguez-Lastra, J. Ziroff, F. Forster, P. Puschnig, L. Dössel, K. Müllen, A. Schöll, F. Reinert, Different views on the electronic structure of nanoscale graphene – planar molecule versus quantum dot, New J. Phys. 14 (2012) 113008, http://dx.doi.org/10.1088/1367-2630/14/11/113008

[9] M. Dauth, M. Wiessner, V. Feyer, A. Schöll, P. Puschnig, F. Reinert, S. Kümmel, Angle resolved photoemission from organic semiconductors: orbital imaging beyond the molecular orbital interpretation, New J. Phys. 16 (2014) 103005, http://dx.doi.org/10.1088/1367-2630/16/10/103005

[10] M. Dauth, T. Körzdörfer, S. Kümmel, J. Ziroff, M. Wiessner, A. Schöll, F. Reinert, M. Arita, K. Shimada, Orbital density reconstruction for molecules, Phys. Rev. Lett. 107 (2011) 193002, http://dx.doi.org/10.1103/PhysRevLett.107.193002

[11] Y. Liu, D. Ikeda, S. Nagamatsu, T. Nishi, N. Ueno, S. Kera, Impact of molecular orbital distribution on photoelectron intensity for picene film, J. Electron Spectrosc. Relat. Phenom. 195 (2014) 287–292, http://dx.doi.org/10.1016/j.elspec.2014.06.003

[12] T. Ules, D. Lüftner, E.M. Reinisch, G. Koller, P. Puschnig, M.G. Ramsey, Orbital tomography of hybridized and dispersing molecular overlayers, Phys. Rev. B 90 (2014) 155430, http://dx.doi.org/10.1103/PhysRevB.90.155430

[13] J. Ziroff, F. Forster, A. Schöll, P. Puschnig, F. Reinert, Hybridization of organic molecular orbitals with substrate states at interfaces: PTCDA on silver, Phys. Rev. Lett. 104 (23) (2010) 233004, http://dx.doi.org/10.1103/PhysRevLett.104.233004

[14] S. Berkebile, T. Ules, P. Puschnig, L. Romaner, G. Koller, A.J. Fleming, K. Emtsev, T. Seyller, C. Ambrosch-Draxl, F.P. Netzer, M.G. Ramsey, A momentum space view of the surface chemical bond, Phys. Chem. Chem. Phys. 13 (2011) 3604–3611, http://dx.doi.org/10.1039/C0CP01458C

[15] M. Wießner, J. Ziroff, F. Forster, M. Arita, K. Shimada, P. Puschnig, A. Schöll, F. Reinert, Substrate-mediated band-dispersion of electronic states in adsorbed molecules, Nat. Commun. 4 (2013) 1514, http://dx.doi.org/10.1038/ncomms2522

[16] M. Wießner, J. Kübert, V. Feyer, P. Puschnig, A. Schöll, F. Reinert, Lateral band formation and hybridization in molecular monolayers: Ntcda on ag(110) and cu(100), Phys. Rev. B 88 (2013) 075437, http://dx.doi.org/10.1103/PhysRevB.88.075437

[17] M. Willenbockel, B. Stadtmüller, K. Schönauer, F. Bocquet, D. Lüftner, E.M. Reinisch, T. Ules, G. Koller, C. Kumpf, S. Soubatch, P. Puschnig, M.G. Ramsey, F.S. Tautz, Energy offsets within a molecular monolayer: the influence of the molecular environment, New J. Phys. 15 (2013) 033017, http://dx.doi.org/10.1088/1367-2630/15/3/033017

[18] B. Stadtmüller, D. Lüftner, M. Willenbockel, E.M. Reinisch, T. Sueyoshi, G. Koller, S. Soubatch, M.G. Ramsey, P. Puschnig, F.S. Tautz, C. Kumpf, Unexpected interplay of bonding height and energy level alignment at heteromolecular hybrid interfaces, Nat. Commun. 5 (2014) 3685, http://dx.doi.org/10.1038/ncomms4685

[19] M. Willenbockel, D. Lüftner, B. Stadtmüller, G. Koller, C. Kumpf, P. Puschnig, S. Soubatch, M.G. Ramsey, F.S. Tautz, The interplay between interface structure, energy level alignment and chemical bonding strength at organic–metal interfaces, Phys. Chem. Chem. Phys. 17 (2015) 1530–1548, http://dx.doi.org/10.1039/C4CP04595E

[20] P. Puschnig, G. Koller, C. Draxl, M.G. Ramsey, Small Molecules on Surfaces - Fundamentals and Applications, Springer, 2013, pp. 1–21, Ch. The Structure of Molecular Orbitals Investigated by Angle-Resolved Photoemission.

[21] D. Lüftner, M. Milko, S. Huppmann, M. Scholz, N. Ngyuen, M. Wießner, A. Schöll, F. Reinert, P. Puschnig, CuPc/Au(110): Determination of the azimuthal alignment by combination of a angle-resolved photoemission and density functional theory, J. Electron Spectrosc. Relat. Phenom. 195 (2014) 293–300, http://dx.doi.org/10.1016/j.elspec.2014.06.002

[22] V. Feyer, M. Graus, P. Nigge, M. Wießner, R. Acres, C. Wiemann, C. Schneider, A. Schöll, F. Reinert, Adsorption geometry and electronic structure of iron phthalocyanine on ag surfaces: a LEED and photoelectron momentum mapping study, Surf. Sci. 621 (0) (2014) 64–68, http://dx.doi.org/10.1016/j.susc.2013.10.020

[23] V. Feyer, M. Graus, P. Nigge, G. Zamborlini, R. Acres, A. Schöll, F. Reinert, C. Schneider, The geometric and electronic structure of TCNQ and TCNQ+Mn on Ag(001) and Cu(001) surfaces, J. Electron Spectrosc. Relat. Phenom. 0 (2015), http://dx.doi.org/10.1016/j.elspec.2015.02.010

[24] E.M. Reinisch, T. Ules, P. Puschnig, S. Berkebile, M. Ostler, T. Seyller, M.G. Ramsey, G. Koller, Development and character of gap states on alkali doping of molecular films, New J. Phys. 16 (2014) 023011, http://dx.doi.org/10.1088/1367-2630/16/2/023011

[25] D. Lüftner, T. Ules, E.M. Reinisch, G. Koller, S. Soubatch, F.S. Tautz, M.G. Ramsey, P. Puschnig, Imaging the wave functions of adsorbed molecules, Proc. Nat. Acad. Sci. U. S. A. 111 (2) (2014) 605–610, http://dx.doi.org/10.1073/pnas.1315716110

[26] M. Wießner, D. Hauschild, C. Sauer, V. Feyer, A. Scholl, F. Reinert, Complete determination of molecular orbitals by measurement of phase symmetry and electron density, Nat. Commun. 5 (2014) 4156, http://dx.doi.org/10.1038/ncomms5156

[27] T. Enoki, T. Ando, Physics and Chemistry of Graphene – Graphene to Nanographene, Pan Standford Publishing, 2013.

[28] K. Nakada, M. Fujita, G. Dresselhaus, M.S. Dresselhaus, Edge state in graphene ribbons: nanometer size effect and edge shape dependence, Phys. Rev. B 54 (1996) 17954–17961, http://dx.doi.org/10.1103/PhysRevB.54.17954

[29] K. Yoshizawa, K. Yahara, K. Tanaka, T. Yamabe, Bandgap oscillation in polyphenanthrenes, J. Phys. Chem. B 102 (3) (1998) 498–506, http://dx.doi.org/10.1021/jp972799f

[30] A. Kuc, T. Heine, G. Seifert, Structural and electronic properties of graphene nanoflakes, Phys. Rev. B 81 (2010) 085430, http://dx.doi.org/10.1103/PhysRevB.81.085430

[31] M. Sola, Forty years of clar's aromatic π-sextet rule, Front. Chem. 1 (2013) 1–8, http://dx.doi.org/10.3389/fchem.2013.00022

[32] S. Fujii, T. Enoki, Clar's aromatic sextet and π-electron distribution in nanographene, Angew. Chem. Int. Ed. 51 (29) (2012) 7236–7241, http://dx.doi.org/10.1002/anie.201202560

[33] N. Wohner, P. Lam, K. Sattler, Energetic stability of graphene nanoflakes and nanocones, Carbon 67 (0) (2014) 721–735, http://dx.doi.org/10.1016/j.carbon.2013.10.064

[34] H.G. Zhang, H. Hu, Y. Pan, J.H. Mao, M. Gao, H.M. Guo, S.X. Du, T. Greber, H.-J. Gao, Graphene based quantum dots, J. Phys.: Condens. Matter 22 (30) (2010) 302001, http://dx.doi.org/10.1088/0953-8984/22/30/302001

[35] S.K. Hämäläinen, Z. Sun, M.P. Boneschanscher, A. Uppstu, M. Ijäs, A. Harju, D. Vanmaekelbergh, P. Liljeroth, Quantum-confined electronic states in atomically well-defined graphene nanostructures, Phys. Rev. Lett. 107 (2011) 236803, http://dx.doi.org/10.1103/PhysRevLett.107.236803

[36] D. Subramaniam, F. Libisch, Y. Li, C. Pauly, V. Geringer, R. Reiter, T. Mashoff, M. Liebmann, J. Burgdörfer, C. Busse, T. Michely, R. Mazzarello, M. Pratzer, M. Morgenstern, Wave-function mapping of graphene quantum dots with soft confinement, Phys. Rev. Lett. 108 (2012) 046801, http://dx.doi.org/10.1103/PhysRevLett.108.046801

[37] F. Craes, S. Runte, J. Klinkhammer, M. Kralj, T. Michely, C. Busse, Mapping image potential states on graphene quantum dots, Phys. Rev. Lett. 111 (2013) 056804, http://dx.doi.org/10.1103/PhysRevLett.111.056804

[38] W. Jolie, F. Craes, M. Petrović, N. Atodiresei, V. Caciuc, S. Blügel, M. Kralj, T. Michely, C. Busse, Confinement of dirac electrons in graphene quantum dots, Phys. Rev. B 89 (2014) 155435, http://dx.doi.org/10.1103/PhysRevB.89.155435

[39] B. Schatschneider, S. Monaco, J.-J. Liang, A. Tkatchenko, High-throughput investigation of the geometry and electronic structures of gas-phase and crystalline polycyclic aromatic hydrocarbons, J. Phys. Chem. C 118 (34) (2014) 19964–21974, http://dx.doi.org/10.1021/jp5064462

[40] Q. Ye, C. Chi, Recent highlights and perspectives on acene based molecules and materials, Chem. Mater. 26 (14) (2014) 4046–4056, http://dx.doi.org/10.1021/cm501536p

[41] N. Ueno, S. Kera, Electron spectroscopy of functional organic thin films: deep insights into valence electronic structure in relation to charge transport property, Prog. Surf. Sci. 83 (2008) 490–557.

[42] H. Yamane, D. Yoshimura, E. Kawabe, R. Sumii, K. Kanai, Y. Ouchi, N. Ueno, K. Seki, Electronic structure at highly ordered organic/metal interfaces: pentacene on cu(110), Phys. Rev. B 76 (2007) 165436.

[43] K. Müller, A. Kara, T.K. Kim, R. Bertschinger, A. Scheybal, J. Osterwalder, T.A. Jung, Multimorphism in molecular monolayers: Pentacene on cu(110), Phys. Rev. B 79 (2009) 245421.

[44] A. Scheybal, K. Müller, R. Bertschinger, M. Wahl, A. Bendounan, P. Aebi, T.A. Jung, Modification of the cu(110) shockley surface state by an adsorbed pentacene monolayer, Phys. Rev. B 79 (11) (2009) 115406, http://dx.doi.org/10.1103/PhysRevB.79.115406

[45] K. Müller, A.P. Seitsonen, T. Brugger, J. Westover, T. Greber, T. Jung, A. Kara, Electronic structure of an organic/metal interface: pentacene/cu(110), J. Phys. Chem. C 116 (2012) 23465–23471, http://dx.doi.org/10.1021/jp308058u

[46] S. Berkebile, P. Puschnig, G. Koller, M. Oehzelt, F.P. Netzer, C. Ambrosch-Draxl, M.G. Ramsey, Electronic band structure of pentacene: an experimental and theoretical study, Phys. Rev. B 77 (2008) 115312, http://dx.doi.org/10.1103/PhysRevB.77.115312

[47] H. Yamane, E. Kawabe, D. Yoshimura, R. Sumii, K. Kanai, Y. Ouchi, N. Ueno, K. Seki, Intermolecular band dispersion in highly ordered monolayer and multilayer films of pentacene on cu(110), Phys. Stat. Sol. (b) 245 (2008) 793–798.

[48] S. Berkebile, G. Koller, A. Fleming, P. Puschnig, C. Ambrosch-Draxl, K. Emtsev, T. Seyller, J. Riley, M. Ramsey, The electronic structure of pentacene revisited, J. Electron Spectrosc. Relat. Phenom. 174 (2009) 22–27, http://dx.doi.org/10.1016/j.elspec.2009.04.001

[49] Q. Xin, S. Duhm, F. Bussolotti, K. Akaike, Y. Kubozono, H. Aoki, T. Kosugi, S. Kera, N. Ueno, Accessing surface brillouin zone and band structure of picene single crystals, Phys. Rev. Lett. 108 (2012) 226401, http://dx.doi.org/10.1103/PhysRevLett.108.226401
[50] J. Repp, G. Meyer, S.M. Stojkovic, A. Gourdon, C. Joachim, Molecules on insulating films: Scanning-tunneling microscopy imaging of individual molecular orbitals, Phys. Rev. Lett. 94 (2005) 026803.
[51] J. Repp, G. Meyer, S. Paavilainen, F.E. Olsson, M. Persson, Imaging bond formation between a gold atom and pentacene on an insulating surface, Science 312 (2006) 1196, http://dx.doi.org/10.1126/science.1126073
[52] W.-H. Soe, C. Manzano, A. De Sarkar, N. Chandrasekhar, C. Joachim, Direct observation of molecular orbitals of pentacene physisorbed on au(111) by scanning tunneling microscope, Phys. Rev. Lett. 102 (2009) 176102, http://dx.doi.org/10.1103/PhysRevLett.102.176102
[53] T. Seyller, K. Emtsev, K. Gao, F. Speck, L. Ley, A. Tadich, L. Broekman, J. Riley, R. Leckey, O. Rader, A. Varykhalov, A. Shikin, Structural and electronic properties of graphite layers grown on sic(0 0 0 1), Surf. Sci. 600 (2006) 3906–3911, http://dx.doi.org/10.1016/j.susc.2006.01.102
[54] K.V. Emtsev, F. Speck, T. Seyller, L. Ley, J.D. Riley, Interaction, growth, and ordering of epitaxial graphene on sic0001 surfaces: a comparative photoelectron spectroscopy study, Phys. Rev. B 77 (2008) 155303, http://dx.doi.org/10.1103/PhysRevB.77.155303
[55] A. Grüneis, K. Kummer, D.V. Vyalikh, Dynamics of graphene growth on a metal surface: a time-dependent photoemission study, New J. Phys. 11 (2009) 073050, http://dx.doi.org/10.1088/1367-2630/11/7/073050
[56] A. Tejeda, A. Taleb-Ibrahimi, W. de Heer, C. Berger, E.H. Conrad, Electronic structure of epitaxial graphene grown on the c-face of sic and its relation to the structure, New J. Phys. 14 (2012) 125007, http://dx.doi.org/10.1088/1367-2630/14/12/125007
[57] T. Haarlammert, L. Bignardi, C. Winter, G. Fecher, P. Rudolf, H. Zacharias, Final-state effects in photoemission experiments from graphene on ni(111), Eur. Phys. J. B 86 (2013) 225, http://dx.doi.org/10.1140/epjb/e2013-40044-1
[58] E.L. Shirley, L.J. Terminello, A. Santoni, F.J. Himpsel, Brillouin-zone-selection effects in graphite photoelectron angular distributions, Phys. Rev. B 51 (1995) 13614.
[59] W.S. Jung, C.S. Leem, C. Kim, S.R. Park, S.Y. Park, B.J. Kim, E. Rotenberg, C. Kim, Imaging the electron density in solids by using multi-brillouin-zone angle resolved photoelectron spectroscopy, Phys. Rev. B 82 (23) (2010) 235105, http://dx.doi.org/10.1103/PhysRevB.82.235105
[60] G. Kresse, J. Hafner, Ab initio molecule dynamics for liquid metals, Phys. Rev. B 47 (1993) 558.
[61] G. Kresse, D. Joubert, From ultrasoft pseudopotentials to the projector augmented-wave method, Phys. Rev. B 59 (1999) 1758.
[62] P.E. Blöchl, Projector augmented-wave method, Phys. Rev. B 50 (1994) 17953.
[63] J.P. Perdew, K. Burke, M. Ernzerhof, Generalized gradient approximation made simple, Phys. Rev. Lett. 77 (1996) 3865.
[64] J. Heyd, G.E. Scuseria, M. Ernzerhof, Erratum: hybrid functionals based on a screened coulomb potential [j. chem. phys. 118, 8207 (2003)], J. Chem. Phys. 124 (2006) 219906, http://dx.doi.org/10.1063/1.2204597
[65] H. Offenbacher, D. Lüftner, T. Ules, E.M. Reinisch, G. Koller, P. Puschnig, M.G. Ramsey, Orbital tomography: molecular band maps, momentum maps and the imaging of real space orbitals of adsorbed molecules, J. Electron Spectrosc. Relat. Phenom. (2015), http://dx.doi.org/10.1016/j.elspec.2015.04.023 (Available online 11 May 2015).
[66] P.J. Feibelman, D.E. Eastman, Photoemission spectroscopy – correspondence between quantum theory and experimental phenomenology, Phys. Rev. B 10 (1974) 4932.
[67] A. Mugarza, J.E. Ortega, F.J. Himpsel, F.J. Garc’íde Abajo, Measurement of electron wave functions and confining potentials via photoemission, Phys. Rev. B 67 (8) (2003) 081404, http://dx.doi.org/10.1103/PhysRevB.67.081404
[68] N. Marom, O. Hod, G.E. Scuseria, L. Kronik, Electronic structure of copper phthalocyanine: a comparative density functional theory study, J. Chem. Phys. 128 (2008) 164107, http://dx.doi.org/10.1063/1.2898540
[69] T. Körzdörfer, S. Kümmel, N. Marom, L. Kronik, When to trust photoelectron spectra from Kohn-Sham eigenvalues: the case of organic semiconductors, Phys. Rev. B 79 (2009) 201205R, http://dx.doi.org/10.1103/PhysRevB.79.201205
[70] D. Lüftner, S. Refaely-Abramson, M. Pachler, R. Resel, M.G. Ramsey, L. Kronik, P. Puschnig, Experimental and theoretical electronic structure of quinacridone, Phys. Rev. B 90 (2014) 075204, http://dx.doi.org/10.1103/PhysRevB.90.075204
[71] J.B. Neaton, M.S. Hybertsen, S.G. Louie, Renormalization of molecular electronic levels at metal–molecule interface, Phys. Rev. Lett. 97 (2006) 216405, http://dx.doi.org/10.1103/PhysRevLett.97.216405
[72] S. Refaely-Abramson, S. Sharifzadeh, N. Govind, J. Autschbach, J.B. Neaton, R. Baer, L. Kronik, Quasiparticle spectra from a nonempirical optimally tuned range-separated hybrid density functional, Rev. Lett. 109 (2012) 226405, http://dx.doi.org/10.1103/PhysRevLett.109.226405
[73] S. Refaely-Abramson, S. Sharifzadeh, M. Jain, R. Baer, J.B. Neaton, L. Kronik, Gap renormalization of molecular crystals from density-functional theory, Phys. Rev. B 88 (2013) 081204, http://dx.doi.org/10.1103/PhysRevB.88.081204
[74] H. Hwang, C. Hwang, Tight-binding approach to understand photoelectron intensity from graphene for circularly polarized light, J. Electron Spectrosc. Relat. Phenom. 198 (0) (2015) 1–5, http://dx.doi.org/10.1016/j.elspec.2014.10.011
[75] C. Ambrosch-Draxl, J.A. Majewski, P. Vogl, G. Leising, First-principles studies of the structural and optical properties of crystalline poly(para-phenylene), Phys. Rev. B 51 (1995) 9668.
[76] P. Puschnig, C. Ambrosch-Draxl, Density-functional study for the oligomers of poly(para-phenylene): band structures and dielectric tensors, Phys. Rev. B 60 (11) (1999) 7891–7898, http://dx.doi.org/10.1103/PhysRevB.60.7891
[77] G. Heimel, P. Puschnig, Q. Cai, C. Martin, E. Zojer, W. Graupner, M. Chandrasekhar, H.R. Chandrasekhar, C. Ambrosch-Draxl, G. Leising, High pressure raman studies on the structural conformation of oligophenyls, Synth. Met. 116 (1–3) (2001) 163–166, http://dx.doi.org/10.1016/S0379-6779(00)00478-1
[78] P. Puschnig, C. Ambrosch-Draxl, G. Heimel, E. Zojer, R. Resel, G. Leising, M. Kriechbaum, W. Graupner, Pressure studies on the intermolecular interactions in biphenyl, Synth. Met. 116 (1–3) (2001) 327–331, http://dx.doi.org/10.1016/S0379-6779(00)00431-8
[79] R. Mitsuhashi, Y. Suzuki, Y. Yamanari, H. Mitamura, T. Kambe, N. Ikeda, H. Okamoto, A. Fujiwara, M. Yamaji, N. Kawasaki, Y. Maniwa, Y. Kubozono, Superconductivity in alkali-metal-doped picene, Nature 464 (2010) 76–79, http://dx.doi.org/10.1038/nature08859
[80] N. Marzari, D. Vanderbilt, Maximally localized generalized wannier functions for composite energy bands, Phys. Rev. B 56 (20) (1997) 12847–12865, http://dx.doi.org/10.1103/PhysRevB.56.12847
[81] N. Marzari, A.A. Mostofi, J.R. Yates, I. Souza, D. Vanderbilt, Maximally localized wannier functions: theory and applications, Rev. Mod. Phys. 84 (2012) 1419–1475, http://dx.doi.org/10.1103/RevModPhys.84.1419.